Shortening Rates and Recurrence of Large Earthquakes From Folded and Uplifted Terraces in the Western Danghe Nan Shan Foreland, North Tibet

Yanxiu Shao, Jerome van der Woerd, Jing Liu-Zeng, Daoyang Yuan, Yunsheng Yao, Xiaobo Zou, Pengtao Wang

Shortening rates and recurrence of large earthquakes from folded and uplifted terraces in the Western Danghe Nan Shan foreland, north Tibet

Yanxiu Shao[1*], Jerome van der Woerd[2*], Jing Liu-Zeng[1], Daoyan Yuan[3], Yunsheng Yao, Xiaobo Zou[4], Pengtao Wang[4]

[1] Institute of Surface-Earth System Science, Tianjin University, Tianjin, 300072 China
[2] Institut Terre et Environnement de Strasbourg ITES UMR7063 Université de Strasbourg, CNRS, ENGEES, 5 rue René Descartes, 67084 Strasbourg Cedex, France
[3] School of Earth Science, Lanzhou University, Lanzhou, 730000 China
[4] Lanzhou Institute of Seismology, China Earthquake Administration, Lanzhou, 730000 China

Corresponding authors: Yanxiu Shao (shaoyx@tju.edu.cn), Jerome van der Woerd (jerome.vanderwoerd@unistra.fr)

Key Points:

- Combined cosmogenic nuclides, OSL, and ^{14}C dating methods constrain the deposition age of four inset folded terraces over the last 130 ka.
- The shortening rate of 0.8 ± 0.2 mm/yr across the western Danghe Nan Shan thrusts is coeval with left-slip decrease along Altyn Tagh fault.
- Concurrent rupture of thrusts and strike-slip fault strands could result in a M*w* 7+ earthquake southwest of Subei town.

Abstract

Understanding the three-dimensional structure, segmentation, and kinematic of complex fault systems are essential to assessing the size of potential earthquakes and related seismic hazards. The Danghe Nan Shan, a major thrust splay of the Altyn Tagh fault in north Tibet, is one of these complex faults junction. Near the town of Subei, the western Danghe Nan Shan thrust is composed of two left-stepping faults outlined by fault scarps in front of folded and uplifted alluvial fans and terraces. Age constraints and 2D reconstructions of the accumulated slip above a transient base level of four terraces standing 7 to 60 m above the present stream bed determine the shortening and vertical uplift rates on the southern thrust of 0.5 ± 0.1 mm/yr and 1.1 ± 0.3 mm/yr, respectively, over the last 130 ka. Along the northern thrust, vertical terrace offsets of 1.5 to 3.6 m and horizontal slip of 4.5 m documented in a paleoseismological trench occurred after 12 ± 4 ka, constraining coeval rates of 0.3 ± 0.1 mm/yr for uplift and shortening. Overall, 1.4 ± 0.4 mm/yr terrace uplift and 0.8 ± 0.2 mm/yr shortening rates are determined, in agreement with late Miocene long-term exhumation rate estimates. Our fault mapping together with geomorphic and structural observations imply that the western Danghe Nan Shan accommodates slip transfer from the Altyn Tagh fault to the west to thrusting and shortening farther east in the Qilian Shan region. Considering the size of the scarps, their lateral extent, the geometry of the faults at depth, and their slip-rate, we suggest the possible occurrence of Mw 7+ earthquakes near Subei.

Plain Language Summary

How faults slip is essential to understanding continental deformation and seismic hazards. In the western Qilian Shan region, the Danghe Nan Shan is one of the largest ranges bounded by active thrust faults. West and south of Subei, these thrusts can be followed for several kilometers along meter-high scarps and folded terraces. Quantifying the cumulative deformation of the folded and uplifted terraces and fans enables to constrain shortening rates of about 1 mm/yr over the last 130 ka. Evidence from surface geomorphology and sub-surface trenching across the faults indicates the occurrence of large magnitude potentially up to M*w* 7 seismic events in the last 16 ka. Integrating age-controlled cumulative geological observations with field-documented co-seismic deformation contributes to increasing the knowledge of slip rate and co-seismic displacement for seismic hazards.

59

1. Introduction

The repetitive nature of earthquake occurrence is a characteristic of faulting behavior, allowing for seismic hazard assessment. While crustal strain can be concentrated and localized along a single fault, some fault systems are highly segmented and distributed, making it more difficult to constrain each fault's behavior. For instance, it has been shown that the Carrizo plain segment of the San Andreas fault concentrates most of the tectonic plate displacement and with 15 recurrent events in the last 1500 years (e.g., Sieh and Jahns, 1984; Weldon et al., 2004; Liu-Zeng et al., 2006). Strike-slip faults produce long single-trace ruptures, like, for example, along the Kunlun fault, with the Manyi (Mw7.6 1997, Peltzer et al., 1999) and Kokoxili (Mw7.9 14/11/2001, Klinger et al., 2005) events, or along the North Anatolian fault (Stein et al., 1997). Thrust or combined strike-slip/thrust events are sometimes more complex, like for instance, the Wenchuan earthquake (Mw7.9 2008; Xu et al., 2009; Hubbard et al., 2010) with two obliquely slipping major thrusts, or the Kaikoura earthquake (Mw7.8 2016; Shi et al., 2019) with a complex combination of thrusts and strike-slip faults or may even stay blind as the recent Himalaya Gorkha earthquake (Mw7.8 2015; Hubbard et al., 2016). It thus requires quantification of fault geometry, activity, and rupture history along adjacent and intersecting fault networks to understand how such complex rupture occurs.

The Qilian Shan region has long been recognized as a crustal-scale restraining step-over between the two northernmost major strike-slip faults at the margin of the Tibetan plateau (Tapponnier and Molnar, 1977; Meyer et al., 1998; Zuza et al., 2018). Left-lateral slip along the N70°E-striking Altyn Tagh fault (ATF) is transferred to the N100°E-striking Haiyuan fault through a set of thrusts and strike-slip faults distributed within the Qilian Shan region. The complex links between strike-slip and thrust faults have been highlighted in some historical earthquakes, such as the Changma event of 1932 (Meyer, 1991; Xu et al., 2010) or the Gulang earthquake of 1927 (Gaudemer et al., 1995; Guo et al., 2020). How thrust faults connect at depth to accommodate strain responsible for folding and mountain building may allow us to assess the rupture area at depth better and thus the magnitude of past and future earthquakes (e.g., Stockmeyer et al., 2014 ; Shi et al., 2019).

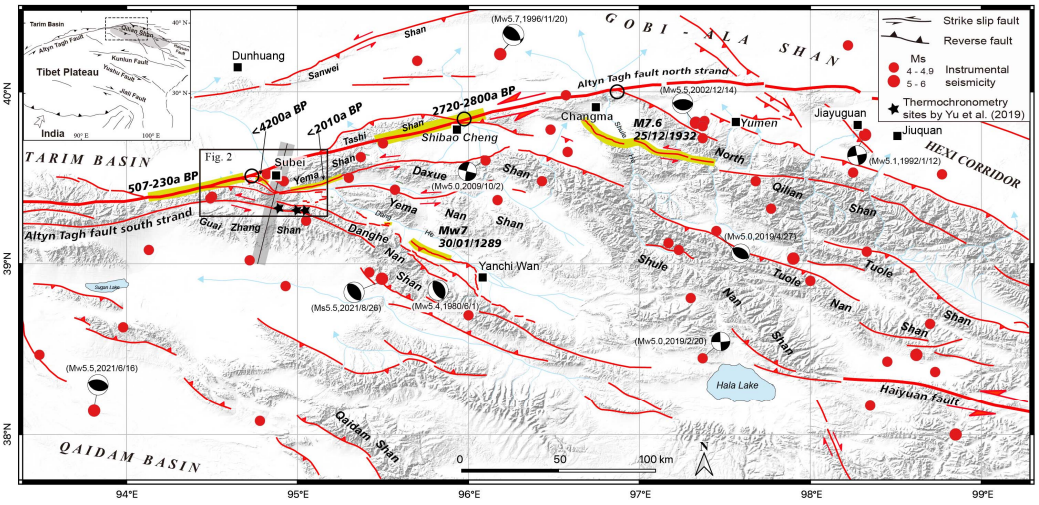

Figure 1. Active faults map of northwestern Qilian Shan region (modified from Tapponnier et al., 1990; Meyer et al., 1998; Van der Woerd et al., 2001). Inset shows location of area in simplified tectonic map of Tibet. Seismicity (magnitude >4) from China Earthquake Networks Center (CENC) catalog (1970 – 2021). Focal mechanisms from GCMT (1970 – 2021). Yellow shaded fault traces with dates are historical and most recent paleo-earthquake rupture extensions from Meyer (1991), Xu et al. (2010), Li et al. (2016), Shao et al. (2017), Wu et al. (2017), He et al. (2018) and Luo et al. (2019). Gray shaded area with black line is position of swath profile in Figure 12. Black circles are major triple junctions along Altyn Tagh fault, Subei, Shibao Cheng/Changma, and Qilian junctions, from west to east.

Along the northwestern Qilian Shan region margin, splays from the Altyn Tagh fault veer eastward and connect with the ranges of Danghe Nan Shan (DHNS), Daxue Shan, and north Qilian Shan, in strike-slip/thrust fault triple junctions (e.g., Meyer et al., 1998; van der Woerd et al., 2001; Xu et al., 2005; Figure 1). The 250 km-long and 20 km-wide DHNS with peaks reaching 5500 m asl, i.e., 4000 m above the Tarim basin to the west and 2000 m above the average elevation of the Qaidam basin, is one of the largest ranges of the Qilian mountains. Its western junction with the ATF, west of the town of Subei, is particularly complex and involves the north and south strands of ATF and several active thrust faults along the northern piedmont of DHNS (Figure 2).

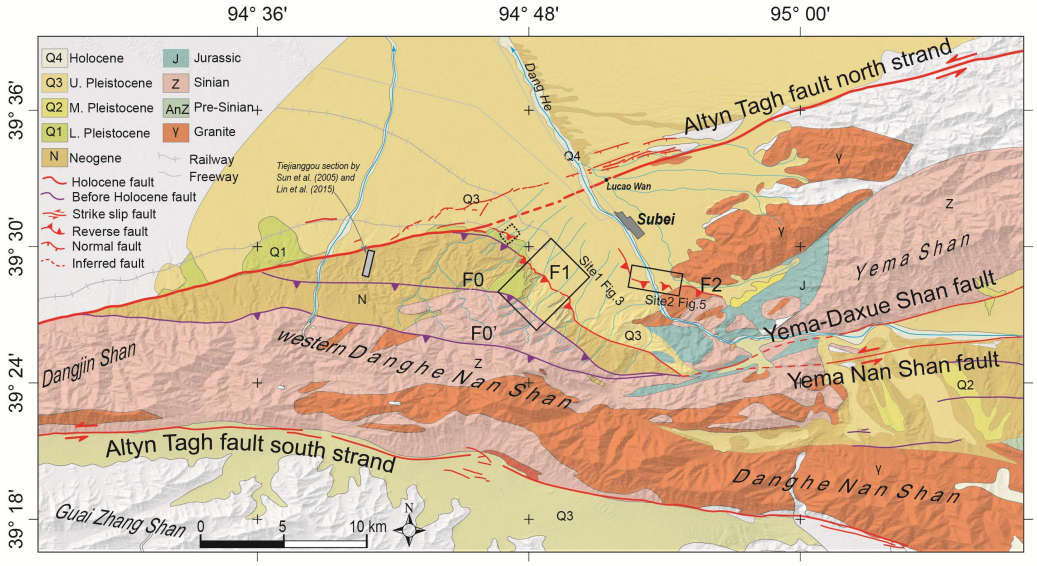

Figure 2. Active fault map at Subei junction from field observations, satellite image interpretation, and topographic data (modified from van der Woerd et al., 2001; see Figure S1). Background is simplified geology from Gansu Bureau of Geology and Mineral Resources of Gansu Province (1989). Main thrusts F0', F0, F1, and F2 are responsible for western Danghenan Shan growth southwest of Subei basin. Open rectangles locate study sites 1 and 2 (Figures 4 and 8). Dashed line rectangle is site 3 of van der Woerd et al. (2001). Grey rectangular box locates palaeomagnetic section in Sun et al. (2005) and Lin et al. (2015).

In this study, we investigate the geometry and the kinematics of active faults at 2 sites along the ~20 km-long western front of the DHNS (sites 1 and 2, Figure 2). Based on topographic profiles of deformed and uplifted terraces, we constrain the sub-surface geometry of the thrust faults and estimate the amounts of uplift and shortening using 2D area balance. We combine several geochronological tools, such as ^{14}C, optically stimulated luminescence (OSL), and terrestrial cosmogenic nuclide (TCN) to date the various terrace levels. Finally, seismic scarp heights and co-seismic slip in trenches, combined with the inferred thrust geometry at depth make it possible to estimate the magnitude of surface rupturing earthquakes generated by the thrust faults.

2. Tectonic setting

The Qilian Shan region at the northern margin of the Tibetan Plateau (Figure 1). is characterized by NW-SE trending thrust and fold belts. These ranges accommodate shortening and confine intermontane basins leading to mountain growth and elevation increase (Burchfiel et al., 1989; Métivier et al., 1998; Meyer et al., 1998; Tapponnier

et al., 1990). Deformation in the Qilian Shan in the Cenozoic results from the collision between Eurasia and India, according to geological structures, palaeomagnetic data and sedimentary records in the Qaidam-Qilian area (e.g., Dai et al., 2006; Dupont-Nivet et al., 2004; Horton et al., 2004; Yin et al., 2002; Yin et al., 2008; Zhou et al., 2006; Zhuang et al., 2011). The Qilian Shan grew during late Oligocene – middle Miocene time (e.g., George et al., 2001; Gilder et al., 2001; Métivier et al., 1998; Zheng et al., 2010) as suggested by magnetostratigraphy, apatite fission-track (AFT) and (U-Th)/He cooling data, and sedimentary mass balance. This growth accelerated during the Pliocene (Métivier et al.,1998) and continued until Quaternary time as evidenced by active thrusting (e.g., Tapponnier et al., 1990; Meyer et al., 1998; Zheng et al., 2013; Hetzel et al., 2004, 2019; Hu et al., 2015, 2021; Du et al., 2020; Xu et al., 2021).

In the western DHNS piedmont, a conglomerate coarsening in the Tiejianggou Formation occurred at 13.7 Ma as determined from palaeomagnetic data (Sun et al., 2005 ; Figure 2). Both changes in sedimentary facies and variations in depositional rates suggest increased tectonic uplift between 13.7 and 9 Ma (Sun et al., 2005). Similarly, the AFT and U-Th/He data obtained from sections of Cenozoic terrestrial clastic sediments and bedrock of Paleozoic granodiorites along the western DHNS (see location in Figures 1 and 2) are consistent with a change in exhumation rate around 14 Ma, implying intensification of uplift at that time (Lin et al., 2015; Yu et al., 2019).

Thrust-fault scarps in the Subei and Yanchi Wan basins, along the western and central DHNS piedmont, respectively, testify to active shortening and surface rupturing earthquakes (Meyer et al., 1998; van der Woerd et al., 2001; Shao et al., 2017; Xu et al., 2021; Figure 1). Thrusting along the western DHNS southwest of Subei is kinematically compatible with a compressive right step between the north strand of ATF and the Yema-Daxue Shan and Yema Nan Shan left-lateral strike-slip faults (Figures 1 and 2). The kinematics of triple junctions predicts that the ATF slip-rate decreases northeastward past the different junctions (e.g., Meyer et al., 1998) as observed by geological and geodetic slip rates distribution along the ATF (Figure S2; Mériaux et al., 2005; Xu et al., 2005; Zhang et al., 2007; Seong et al., 2011; Xiao et al., 2017; Elliott et al., 2018; Liu et al., 2020). Locally, other rates have been determined on thrust or strike-slip faults (van der Woerd et al., 2001; Luo et al., 2015; Zheng et al., 2013; Xu et al., 2021).

A few paleoseismic trenches have been dug along the DHNS thrust and adjacent strike-slip faults. West of the Subei junction, Li et al. (2016) described evidence for four events from a trench dug across the Aksay segment of the ATF. They constrained the ages of two events at 1180 a B.P. and 507 – 230 a B.P. To the east, three events are identified in trenches near Shibao Cheng over the last 7000 years, with the most recent one between 2720 and 2800 a B.P. (Luo et al., 2019). Along the western DHNS (site 3 in Figure 2), a thrust rupture with a vertical offset of ~1.7 m after 4300 a B.P. is documented (Wu et al., 2017). Along the central DHNS in the Yanchi Wan basin (Figure 1), Shao et al. (2017) used high-resolution topographic data and trenches to describe a late event that ruptured between A.D. 1289 and 1395, with horizontal shortening of ~1.3 m, inferred to be the A.D. 1289 event that occurred during the Yuan Dynasty according to historical records. Along the Yema-Daxue Shan fault, He et al. (2018) excavated three paleoseismic trenches and found evidence of three events since 7000 a B.P., with the latest event occurring after 2010 ± 30 a B.P.

Recent seismicity in the western Qilian Shan region is mostly characterized by moderate earthquakes (Figure 1). For instance, nine earthquakes with magnitudes of M4 – 6 have occurred along the DHNS since 1960. The focal mechanisms of these earthquakes are both thrust and strike-slip. A M5.5 earthquake occurred recently on 26 Aug. 2021 with an epicenter along the southern piedmont of DHNS. Its focal mechanism is similar to the Mw5.4 1980 event and, given the uncertainty in hypocenter depth and location, compatible with faulting along north-dipping thrusts subparallel to the range. The largest known event in the area is the 25 December 1932 M7.6 Changma earthquake (Figure 1). The surface rupture of this earthquake extends for 120 km with coseismic horizontal displacements up to 5.5 m (Du et al., 2020; Meyer, 1991; Peltzer et al., 1988). The potential for a large earthquake is suspected in the Subei basin along the DHNS as large several-meter-high seismic scarps are evidenced (see below).

3. Methods

3.1. Shortening constraints from uplifted area balancing

Abandoned, uplifted, and folded terraces may be used to constrain the kinematics of shortening over the time span of the terrace ages (e.g., Meyer et al., 1998; Rockwell et al., 1998; Lavé & Avouac, 2000; van der Woerd et al., 2001; Thompson et al., 2002; Daëron et al., 2007; Simoes et al., 2007; Hu et al., 2015, 2021; Guilbaud

et al., 2017; Xu et al., 2021). Provided that the base levels can be reconstructed, the present height of the strath terraces above their base level is an estimate of the tectonic throw on the underlying thrust fault (e.g., Bull, 1991; Merritts et al., 1994; Lavé and Avouac, 2000; van der Woerd et al., 2001; Thompson et al., 2002; Wang et al., 2020). Using a mass conservation model (Figure 3) and assuming negligible erosion of the terrace, it is possible to estimate the amount of corresponding slip on the thrust fault at depth (S) to account for uplift and folding of the strath level (areas A1 and A2).

We infer the geometry of the thrust fault at depth from the surface geology and structural data, such as bedding of the sedimentary beds or fault dip, similarly to Meyer et al. (1998), van der Woerd (1998), or Hu et al. (2015). We consider a simple geometry of the thrust fault at depth made of two connected planes, a sub-horizontal décollement, and a ramp (Figure 3). The dip of the frontal ramp without surface observation of the emerging thrust fault, may range between 45±15° as commonly observed or inferred from structural data, i.e., bedding of the thrusted sediment layers (e.g., van der Woerd et al., 2001; Gilder et al., 2001). The wavelength of the antiformal folding of the terraces may be used to constrain the depth where the ramp and the décollement meet (D_0; Figure 3, e.g., Meyer et al., 1998). The precise dip (α) or rooting depth (D_α) of the décollement is unknown, thus we use two end-member models, where the dip of the "flat" changes from near 0° (Model 1) to a certain dip (Model 2, $0 < \alpha < 45°$; Figure 3). In Model 1, this depth remains constant until it eventually joins with other faults at depth. In Model 2, the décollement dips with an angle α and thus connects with other faults deeper (Figure 3).

In the case where several terrace levels are incrementally uplifted and folded, and without independent structural constraints on the geometry of the décollement, it is possible to adjust the dip angle α and thus depth D_α by minimizing the shortening rate variations among the terraces. A sloping décollement has two consequences. First, the dipping décollement acts like a shallowly dipping ramp with uniform uplift (U in Model 2, Figure 3) above its entire length (e.g., Meyer et al., 1998; Hu et al., 2015). Second, increasing D_α reduces the slip amount (S) necessary to account for the uplifted area (A2) above base level.

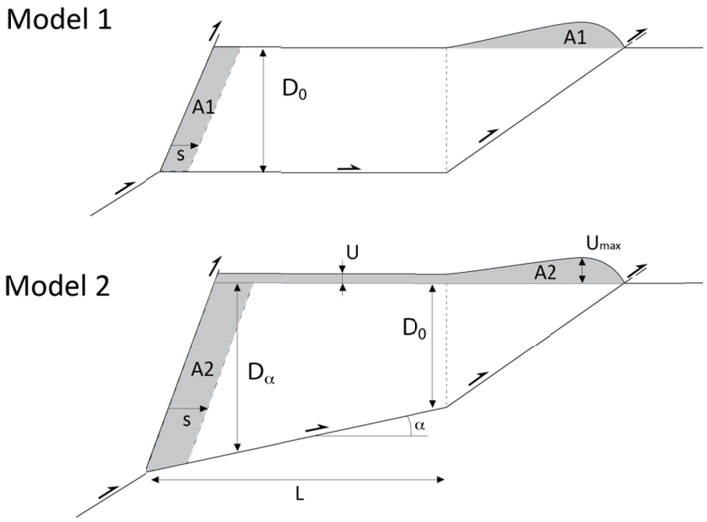

Figure 3. Simplified geometry of ramp and décollement in models 1 and 2 with corresponding parameters (see text). Décollement remains flat in Model 1 while it dips with angle α in Model 2.

3.2. Topographic survey of uplifted landforms

We used different tools to survey the topography of the terrace surfaces and associated riverbeds. At site 1, we levelled 5 – 1600 m-long differential global position system (DGPS) profiles. The rover of the GPS instrument records one position every second. After post-processing, the horizontal and vertical accuracies of the position are approximately 5 and 10 mm, respectively. These profiles are combined with 4 profiles surveyed in 1996 with a digital-recording theodolite-distancemeter with similar sub-cm precision (see details in van der Woerd et al., 2001; Figures 2, 4 and 5). Given the precisions of both instruments, the roughness and irregularities of the several-meter loess-covered terrace surfaces or cobble-rich riverbeds are the primary sources of errors.

We used a drone-based laser scanning to survey the topography at site 2 (Figures 6 and 7). The drone has eight rotors with a VLP16 Velodyne® laser sensor flying at ~50 m above the surface. Millions of cloud points are processed to produce a 0.5 m-resolution digital elevation model (DEM). Vegetation was removed by point classification (Figure 6c).

Chinese ZY-3 satellite stereo-pair images, with a resolution of ~2.5 m (acquired in December 2017), were used to generate a DEM with a horizontal and vertical resolution of ~6 m across the Subei basin (Figure S1).

3.3. Paleoseismic trenching

To document the subsurface fault geometry and rupture history of the seismic scarp at site 2, we investigated the subsurface sedimentation and structure by opening a trench across the main fault scarp (Figures 6 and 7). The exposed walls in the trench are cleaned and photographed with a digital camera (Figure 8). We used the structure-from-motion method to mosaic the photos (e.g. Bemis et al., 2014; Reitman et al., 2015) before mapping the deformed and offset sedimentary units onto the orthophotos.

3.4. Sampling and dating methods

To constrain the age of the deformed terraces and fans, we combined three different dating techniques: terrestrial cosmogenic nuclide (TCN) dating, accelerator mass spectrometry for radiocarbon samples (AMS ^{14}C) and optically stimulated luminescence dating (OSL).

AMS ^{14}C and OSL were used to constrain the ages of sandy or silty sediments found either capping the coarser conglomeratic material of the alluvial deposits or sandy lenses in coarser sediments. The radiocarbon samples were processed and dated at Beta Analytic. Ages were calibrated with IntCal13 (Reimer et al., 2013). All OSL samples were processed and measured following the procedure described in Shao et al. (2017). Fine-grained (4 – 11 μm) quartz fractions were prepared and treated with 30% hydrogen peroxide (H_2O_2) and 10% hydrochloric acid (HCl) to remove organic materials and carbonates, respectively. The purity of the prepared quartz was checked by the ratio of infrared-stimulated luminescence (IRSL) to blue light-stimulated luminescence (BLSL) (<5%). We used a Risø TL/OSL-DA-20 reader equipped with a 90Sr/90Y beta source (~0.12 Gy/s), blue LEDs (470 ± 20 nm, ~80 mW/cm2), and two Hoya U340 filters (290 – 370 nm) to conduct irradiation, heating, and luminescence measurements. A simplified multiple aliquot regenerative dose (SMAR) was used to measure the quartz aliquots.

At site 1, depth profiles are dug into the loess covered surfaces of the terraces in relatively flat places away from any visible surface erosion or incised channels (Figure 4), except for one terrace, where the depth profile was sampled by refreshing its steep eastern riser (Figure 9). From each profile, we collected 6 – 8 samples of quartz-rich gravels in the top 2 m of the several meter-thick gravels/cobbles deposits (Figures 9 and 10). The age of abandonment of the underlying conglomerate is then determined by ^{10}Be depth profile modeling considering shielding of the overlying loess cover, which age is constrained with ^{14}C and OSL dating, following the approach developed in Shao et al. (2021). At site 2, only surface samples were

collected from a boulder fan surface. Six 2.5 cm-thick rock samples were collected with a chisel and hammer from the top of six embedded granitic boulders (size > 0.5 m in diameter) (Figure 11).

The TCN samples were crushed and sieved, allowing the 250 – 500 µm fraction to be treated by sequential ultrasonic leaches to obtain pure quartz. Beryllium oxide was extracted by chromatography from the sample solution and inserted into target holders at the Cosmogenic Isotope Laboratory of Institut Terre et Environnement de Strasbourg (ITES UMR7063). The isotopic ratios were determined at the ASTER-AMS facility at the Centre Européen de Recherche et d'Enseignement des Géosciences de l'Environnement (CEREGE, Aix-en-Provence, France). We used the online calculator of CRONUS-Earth calculator Version 3 (Balco et al., 2008) to calculate the exposure ages of surface samples with the time-dependent scaling model of Lal (1991)/Stone (2000). For subsurface samples, we modeled the ages based on the depth dependence of the concentration (e.g., Braucher et al., 2003; Gosse & Phillips, 2001; Lal, 1991; Yang et al., 2019; Shao et al., 2021). The terrace conglomerate densities, which depend on composition, grain size and consolidation of terrace sediment were estimated from the exponential best fit of the depth profiles. We performed forward modeling to estimate the shielding effect of loess considering a density of 1.4 g/cm^3 and constant accumulation rates calculated by linearly fitting the age/depth relationship from up to three OSL and/or ^{14}C dates (similarly to other studies in the Qilian Shan area, e.g., Hetzel et al., 2004, 2019; Shao et al. 2021).

4. Results

The study sites 1 and 2 are situated in the DHNS bajada south of Subei along the main thrusts F1 and F2 (Figure 2). The first site (site 1) is located in the middle of the uplifted ledge at a place already described in van der Woerd et al. (2001) and composed of a set of four main uplifted and folded terrace levels by thrust F1 (Figure 4). The second site (site 2) is located 10 km to the east along the fault scarp of F2 crossed by the Dang He river.

4.1. The geometry of uplifted and folded alluvial surfaces

4.1.1. Site 1

Southwest of Subei, thrust F1 sharply disrupts the bajada to form a NW-SE trending topographic scarp. Upstream of the scarp, uplifted reaches of late Pleistocene

strath terraces are deposited unconformably above Tertiary reddish sandstones and conglomerates. Variably thick loess covers the sediments of the terraces. Two to three kilometers further southwest, the terraces are overthrust by the steeply faceted Paleozoic bedrock of the DHNS along thrust F0 (Figure 2; van der Woerd et al., 2001). As a response to recent and active uplift, numerous streams have grown into subparallel catchments of relatively small size, deeply incising across the uplifted ledge and depositing alluvial fans in front of thrust F1. While older deposits are preserved upstream as narrow terrace remnants, downstream, younger deposits have buried the older sediments (van der Woerd et al., 2001).

Site 1 is located in the central part of thrust F1 along a stream of one of the largest catchments along the range front (stream r5 in van der Woerd et al., 2001). A set of four terraces (T1 to T4) are preserved upstream of F1, whereas on the downstream side, only one main fan level (Tf2) is present (Figure 4). To constrain the geometry of uplifted and folded terraces upstream of F1, a set of topographic profiles has been leveled along different terraces on the western bank of stream r5 (Figure 4). All profiles are projected in a N45°E direction perpendicular to the average N135°E strike of thrust F1 in Figure 5.

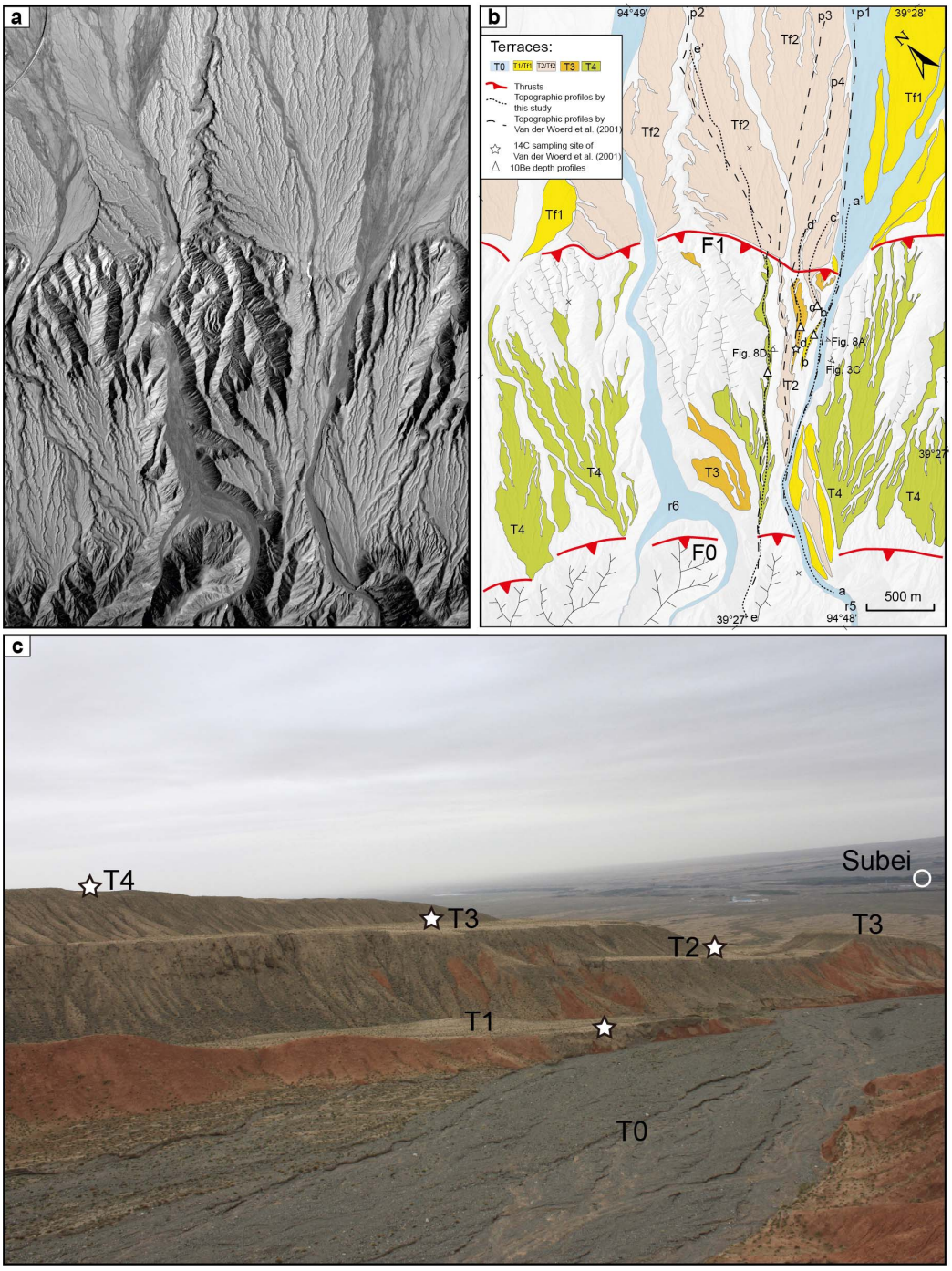

Figure 4. Uplifted and folded terraces along fault F1 at site 1. (a) ZY3 satellite image of site 1. (b) Geomorphic interpretation from image in A and field observations. South of main thrust fault F1, four main terrace levels T1 to T4 are abandoned by stream r5. Dashed and dotted lines are topographic profile locations acquired with total station (van der Woerd et al., 2001) and DGPS (this study), respectively (see Figure 5). Triangles are pit locations for cosmogenic isotope depth profile dating. Star is charcoal sample location in van der Woerd et al. (2001). (c) Field view to north of uplifted and folded terraces at site 1 south of Subei. Terraces are loess covered several-meter-thick greyish conglomerate unconformable on red-orange south dipping

362 Tertiary sandstones and conglomerate. Stars locate sampling pits in terraces T1, T2,
363 T3 and T4.
364

365 From the range front in the south to the bajada in the north, i.e., between F0 and
366 F1 (Figure 4), all terraces show a similar pattern of uplift and deformation. Upstream
367 they stand above the present stream bed with a slightly steeper slope as T0, while they
368 form a clear antiform near their northern end (Figure 5). This shape is particularly
369 clear for T4 and T2, which treads extend largely upstream, while for T1 and T3 only
370 the folded bulge to the north remains. Minimum and maximum heights of terraces T1,
371 T2, T3 and T4 above the present-day stream bed are 0, 18 ± 1, 27 ± 2, and 50 ± 3 m
372 and 7. ± 0.5, 23 ± 1, 40 ± 2, and 60 ± 3 m, respectively (Figure 5; Table 1). From our
373 mapping (Figure 2), the bajada in front of the fold are fan deposits (Tf2)
374 corresponding mostly to terrace level T2. The corresponding maximum offset of the
375 surface T2 relative to the Tf2 bajada is 15 ± 1 m (Table 1).

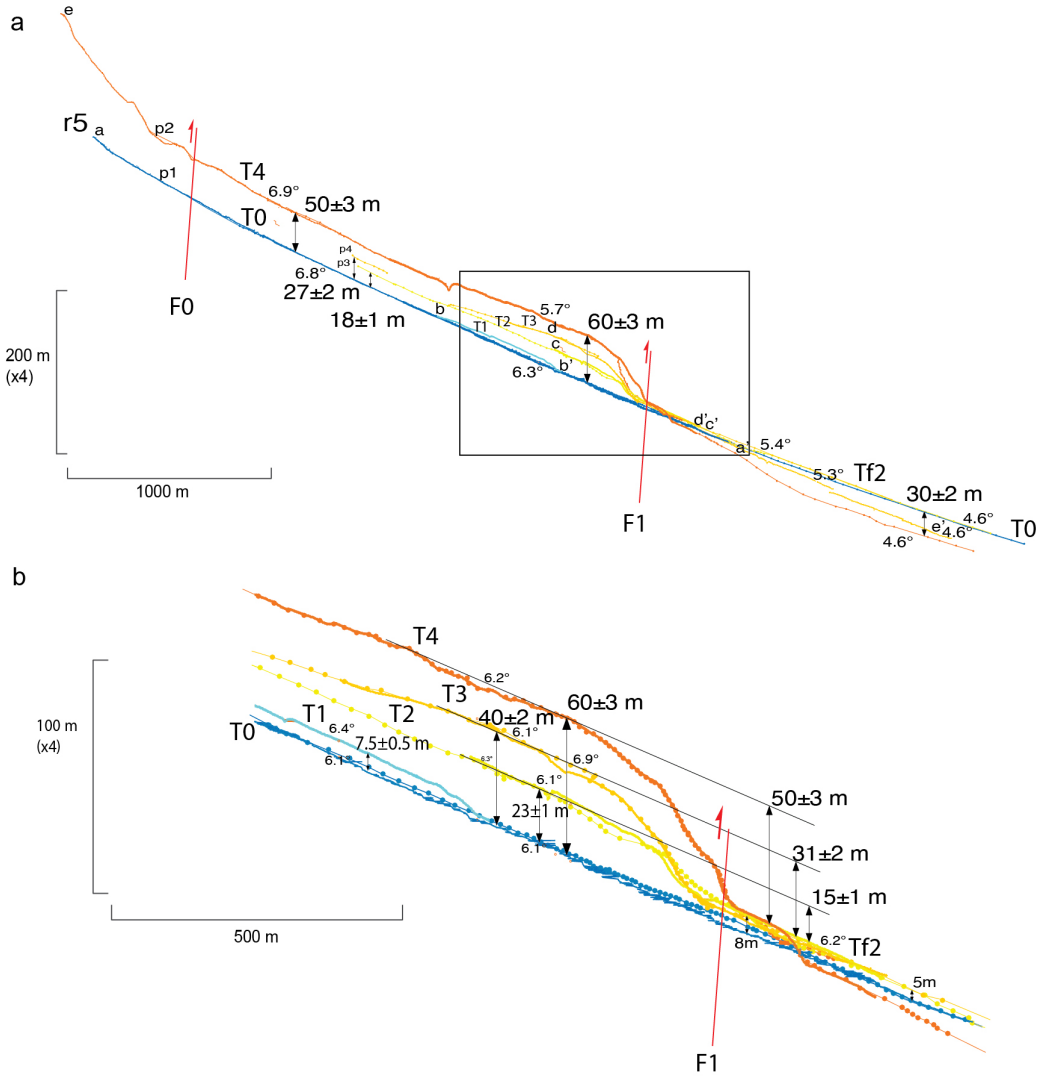

Figure 5. Uplift measurements at site 1. (a) N45°E projected topographic profiles (see location in Figure 4, same labels). Terrace heights measured above active stream bed T0. Main thrust position inferred. (b) Detail of folded terraces at ledge front. Fan Tf2 in footwall corresponds to T2 in the hanging wall. Terrace maximum heights measured above active stream bed T0 in hanging wall and above Tf2 in footwall.

4.1.2. Site 2

Site 2 is located at the bottom of the Subei basin along the Dang He river-bed, approximately 7 km east of site 1 (Figures 2, 5, 6). There, thrust F2 can be traced for approximately 10 km outlined by a series of half-meter- to several-meter-high scarps. To the northwest, the scarps, across the distal fans of the main bajada, are subparallel to F1 for 2 km (Figure 2). The scarps then veer eastward to strike east-west on average across a set of fans abandoned by the Dang He and a major tributary. Site 2 is located where the scarps reach up to several meters high. Farther east, the scarps

continue along the southern rim of a major valley within the Yema Shan, and their traces become unclear in the high relief eastward.

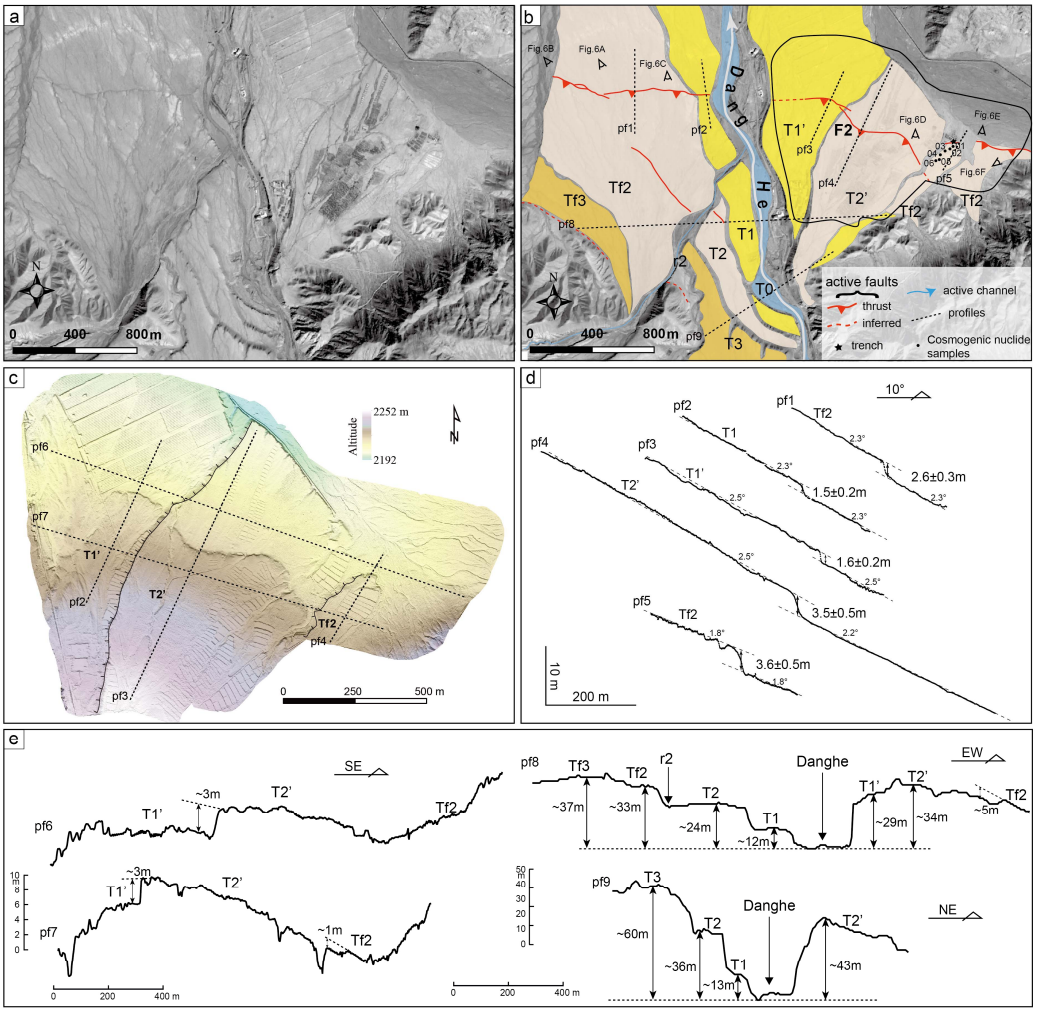

Figure 6. Geomorphic interpretation of site 2. (a) ZY3 satellite image of site 2. (b) Geomorphic map. Black outline is drone based Lidar survey in (c). Dang He has abandoned a set of terraces T1, T1', T2, T2' and T3 as it leaves its gorge across southwest Yema Shan. Tf2 and Tf3 are alluvial fans from smaller tributaries. Terraces and fans are cut and offset by active thrust F2 (in red). (c) High resolution (0.5 m) DEM from drone based Lidar survey. Dashed lines are topographic profiles in (d) and (e). Solid lines represent terrace riser tops, ticks are on lower side. (d) Topographic profile across F2 scarps. Piercing lines (dashed) fit far field slopes of surfaces. (e) Left, topographic profiles extracted from ~6 m resolution DEM, and right, from drone DEM, located in (b) and (c), respectively.

The Dang He and tributaries at site 2 incise in a set of imbricated fans, the oldest and highest fans (T3, Tf3) standing up to 60 m above the riverbed near their apex or where the Dang He leaves the gorge to the east (profiles pf8, pf9; Figure 6). Their slopes decrease progressively from the oldest to youngest. Presently, F2 thrust scarps

409 cut through the lower parts of Tf3, Tf2, T1 and T2'. Across Tf2 and T2', the scarps
410 heights range from 2.6 to 3.5 m, while across T1, the scarp is approximately 1.6 m
411 high (Figure 6D).

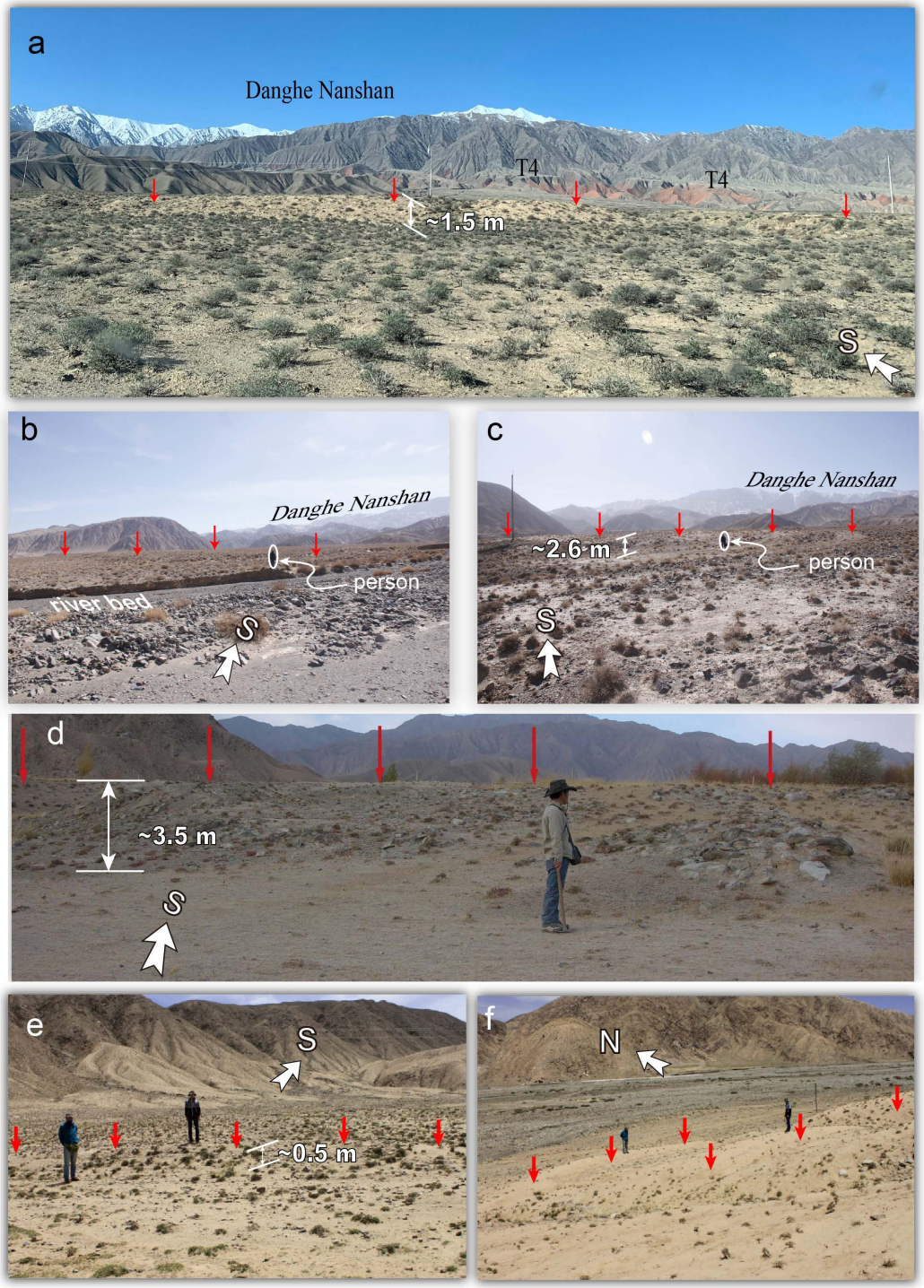

412

413 Figure 7. Field views of faulted alluvial fans and terraces by thrust F2 at site 2 (See
414 Figure 6 for locations). Small arrows indicate top of fault scarp. Person is ~1.7 m tall..
415 (a)-(c) ~1 – 2 m-high scarp west of Dang He. (c) ~2.6 m-high scarp across Tf2. (d)

~3.5 m-high scarp across Tf2. (e) ~0.5 m-high scarp across Tf2. (f) Multiple scarps across 4 m-high faulted and folded terrace front.

The frontal 3.5 ± 0.2 m-high scarp on surface Tf2 (profile pf5; Figure 6D) was targeted for trenching (Figure 8). Orthophotos of the two 13 m-long and 3.5 m-high trench walls exhibit similar units and faulting evidence. Three main units can be separated. Unit 1 (U1) is the top layer of approximately 1 m-thick silty loess thinning upstream, underlain by a 3 – 5 cm thick bed of reddish coarse sand at the bottom. Unit 2 (U2) consists of approximately 1.5 m-thick light gray poorly sorted angular sandy gravels. Unit 3 (U3) is a layer of gray, poorly sorted angular sandy gravels.

Three main shallow-dipping (7° to 19°) thrust faults (f1-f3) can be seen on both walls cutting through units U1 to U3, with a minor back thrust splaying from f2 (Figure 7c). All three faults offset the top of unit U2; faults f2 and f3 also offset the loess unit U1. As a results, the bottom of U2 is displaced ~50 – 55 cm and ~300 – 310 cm by f1 and f2, respectively. The top of U2 is displaced ~50 cm, ~280 cm, and ~90 – 120 cm by f1, f2, and f3, respectively.

Trench exposures show evidence of two events. The older event is indicated by a gravelly colluvial wedge in the footwall of fault f1, occurring before the deposition of unit U1. The younger event is manifested by faults f2 and f3, which offset the base of unit U1. The upward extending traces of faults f2 and f3 are unclear in the homogeneous loess unit. Therefore, it is difficult to determine whether there is more than one event after the deposition of the lower part of unit U1.

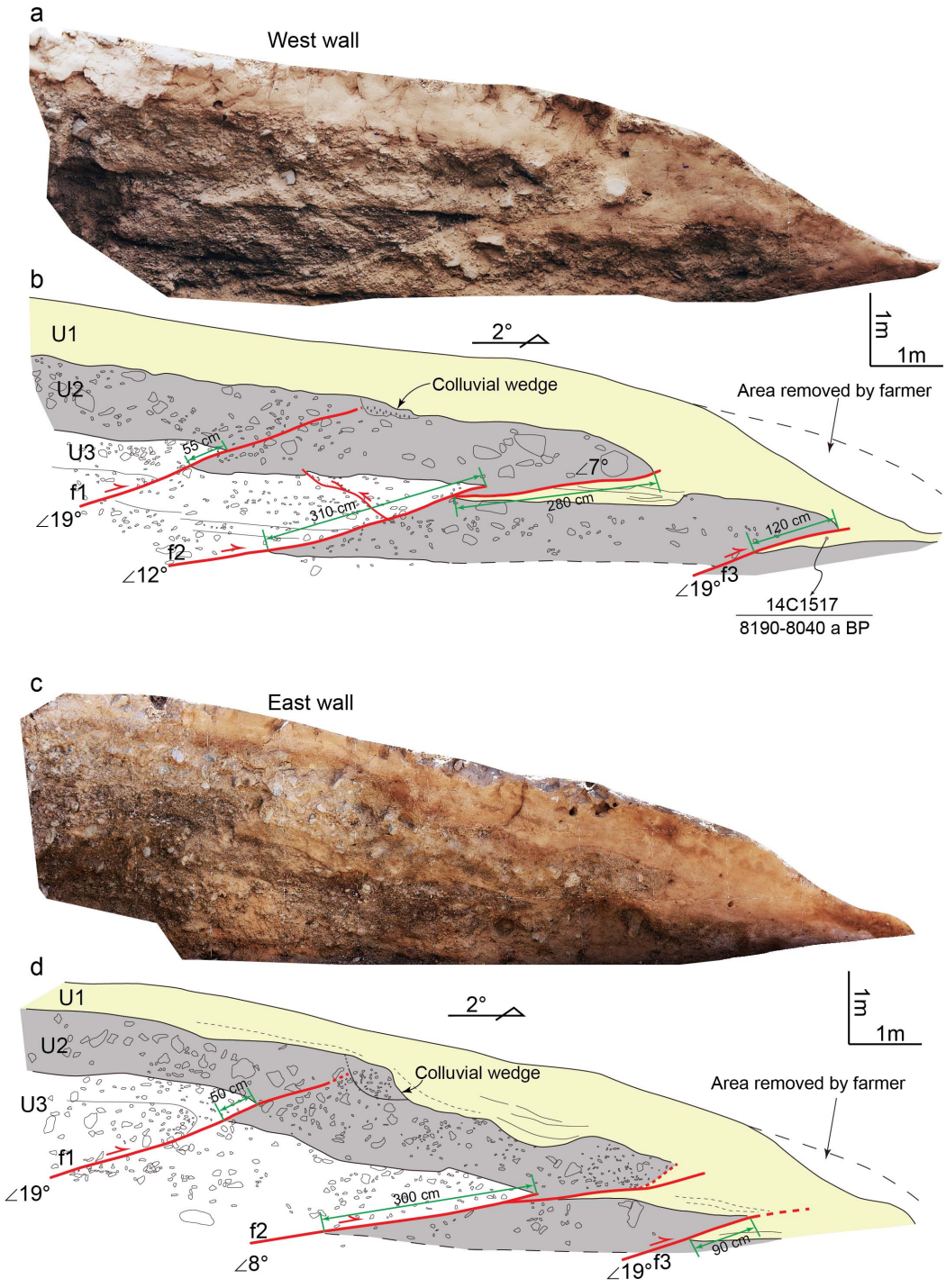

Figure 8. Trench walls photo mosaic (a, c) and interpretation (b, d) at Site 2 (see location in Figure 5). East wall (c and d) is mirrored. Three main units U1, U2 and U3 are faulted. Solid and dashed thin black lines are minor layers. Red lines f1, f2 and f3 are shallow dipping faults, dashed when inferred. Offsets of units are indicated in green. Charcoal sample and calibrated age is indicated (Table 4). See text for unit details.

Taking a 20° dip, the summed dip slip of approximately 4.9 ± 0.2 m of the thrusts

447 in the trench would account for 1.7 ± 0.2 m of uplift. This value is less than half of the
448 3.6 ± 0.2 m height of the frontal scarp of terrace Tf2 (profile pf5 in Figure 6). For
449 these faults and slip amounts to be responsible for the 3.6 ± 0.2 m-high cumulative
450 scarp of Tf2, they must steepen rapidly south of the trench to approximately 47°.
451
452 4.2. Terrace age determination
453 At site 1, we model the exponential depth distribution of ^{10}Be concentrations of
454 amalgamated samples to determine the exposure ages. To average the variable
455 inheritance among the individual rock pieces, our samples include a minimum of 60
456 distinct pebbles, a number usually considered large enough for this purpose (e.g.,
457 Anderson et al., 1996; Hancock et al., 1999; Matrau et al., 2019; Shao et al., 2021).
458 Nevertheless, our depth profiles show scattered ^{10}Be concentrations with depth not
459 simply modeled by an exponential fit. With scattered values largely above analytical
460 errors and in the absence of vertical mixing, several reasons could be responsible for
461 the dispersion observed, such as sequential deposits or not well-averaged inheritance
462 (e.g., Perrineau et al., 2011; Le Dortz et al., 2012). There are no field evidence for
463 sequential deposits or unconformities within the conglomerates. Consequently, in the
464 case of not well-mixed inheritance, the less concentrated samples in the profile are
465 likely closer to the actual terrace exposure time (e.g., Le Dortz et al., 2012). Figure 10
466 shows modeling fitting the less concentrated samples. Model solutions showing an
467 average fit of all samples are also presented in Figures S3 – S6. Both models give
468 similar results with differences up to 10%, which remain small with no systematic
469 bias. We thus present our results below with our preferred modeling considering not
470 well averaged inheritance.
471

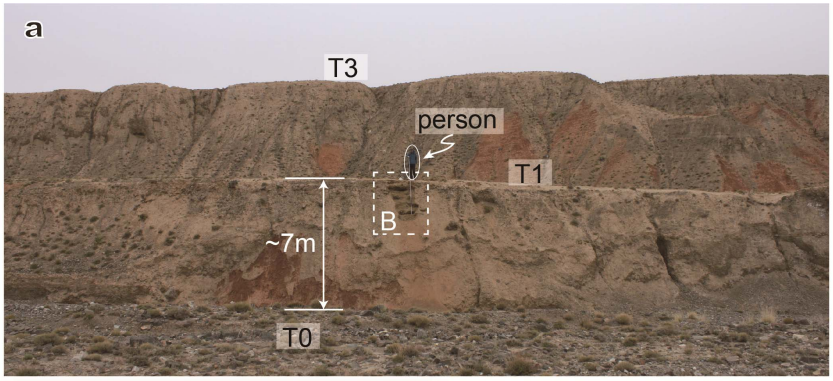
a
T3
person
T1
B
~7m
T0

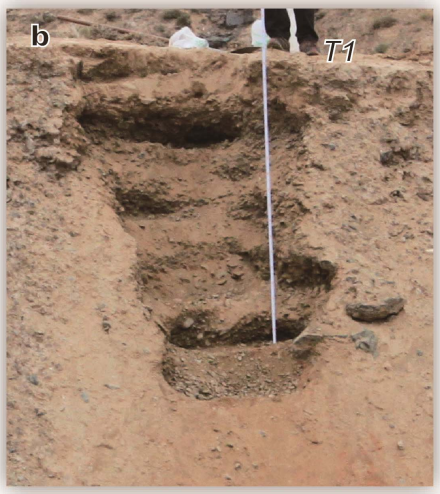
b
T1

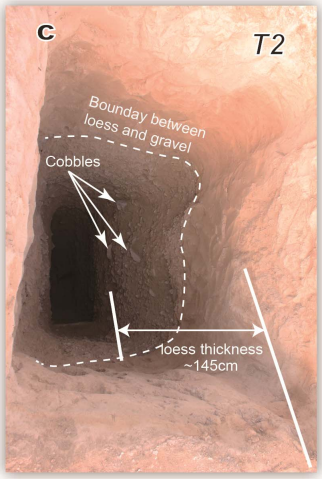
c
T2
Bounday between loess and gravel
Cobbles
loess thickness ~145cm

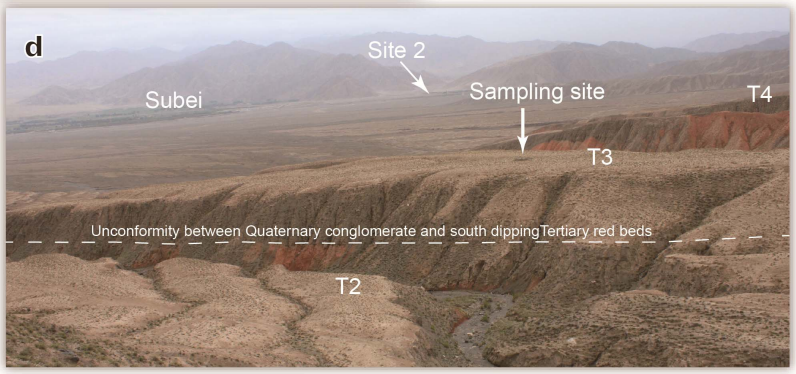
d
Site 2
Subei
Sampling site
T4
T3
Unconformity between Quaternary conglomerate and south dippingTertiary red beds
T2

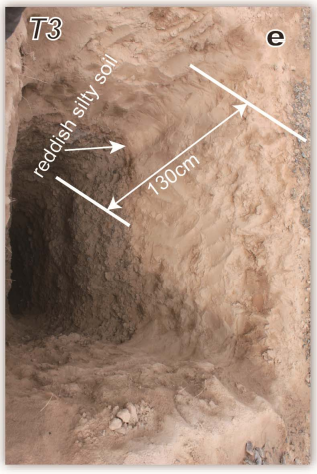
T3
e
reddish silty soil
130cm

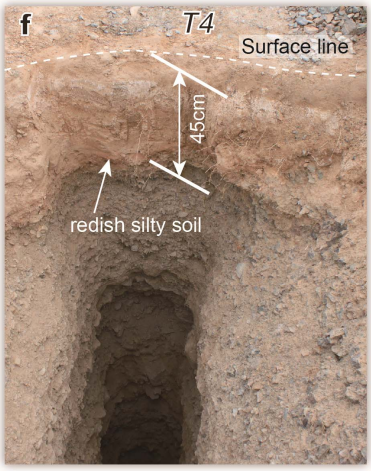
f
T4
Surface line
45cm
redish silty soil

472

Figure 9. Field views of terraces and sampling sites at site 1 (locations of views and pits in Figure 4). (a) Westward view across T1 and T3. Position of depth profile in top 2 m of a loose conglomerate in T1, 7 m above the river bed. Orange colored outcrops below unconformable grey surface conglomerate are south-dipping Tertiary red beds. (b) Close-up view of depth profile in T1. Sandy gravels and pebbles are collected every 20 cm along the profile. (c) Pit dug in terrace T2. Conglomerate is capped by 145 cm-thick loess deposit. (d) Landscape view taken from upper terrace T4 eastward across site 1, Subei county in background left, and site 2 to the right. Location of pit dug in T3 indicated. (e) View of sampling pit in T3 with top 130 cm-thick loess, separated from bottom conglomerate by a reddish silty soil layer. (f) 3 m-deep pit in terrace T4. The top 45 cm-thick layer is made of loess covering a few cm-thick reddish silty soil.

The depth profile in T1 includes 7 samples in the 2 m-thick deposit, which consist of a 20 cm-thick gravel deposit on top of a 10 cm-thick loess layer above a homogenous 1.7 m-thick conglomerate (Figure 10a). An OSL sample from the loess layer yields a date of 5.4 ± 0.2 ka, which we interpret as a minimum age of the terrace (Table 2). The best fit to the ^{10}Be concentration with depth explains four out of seven samples (R^2 = 0.99) and yields a model age of 8.7 ± 0.5 ka. The modeling suggests two depositional phases: a first phase of conglomerate accumulation since 8.7 ± 0.5 ka; after a hiatus, a second phase of 10 cm-thick loess accumulation since 5.4 ± 0.2 ka, and the gravel layer on top (Figure 10b). In the following, we use the 8.7 ± 0.5 ka as the age of T1 as it represents the major phase of terrace formation and because the top loess and gravel layer may post-date the onset of folding and could be derived from post-depositional surface reworking.

A ~3.6 m-deep pit in T2 reveals a loess layer of 145 cm above the conglomerate of the terrace (Figure 10c). Three OSL samples at depths of 50, 90, and 135 cm yield dates of 4.8 ± 0.2, 5.6 ± 0.2, and 5.9 ± 0.2 ka, respectively (Table 2). The samples are stratigraphically ordered, which implies that the 145 cm-thick loess deposits accumulated between 6.1 ka and 4.3 ka at a rate of ~72 cm/kyr. Because the ^{10}Be concentrations of 5 conglomerate samples distributed between 1.5 and 3.5 m depths are scattered, we fit only the 2 less concentrated samples at 1.5 and 2 m depths, thus yielding an exposure age of 9.5 ± 1 ka (Figure 10d).

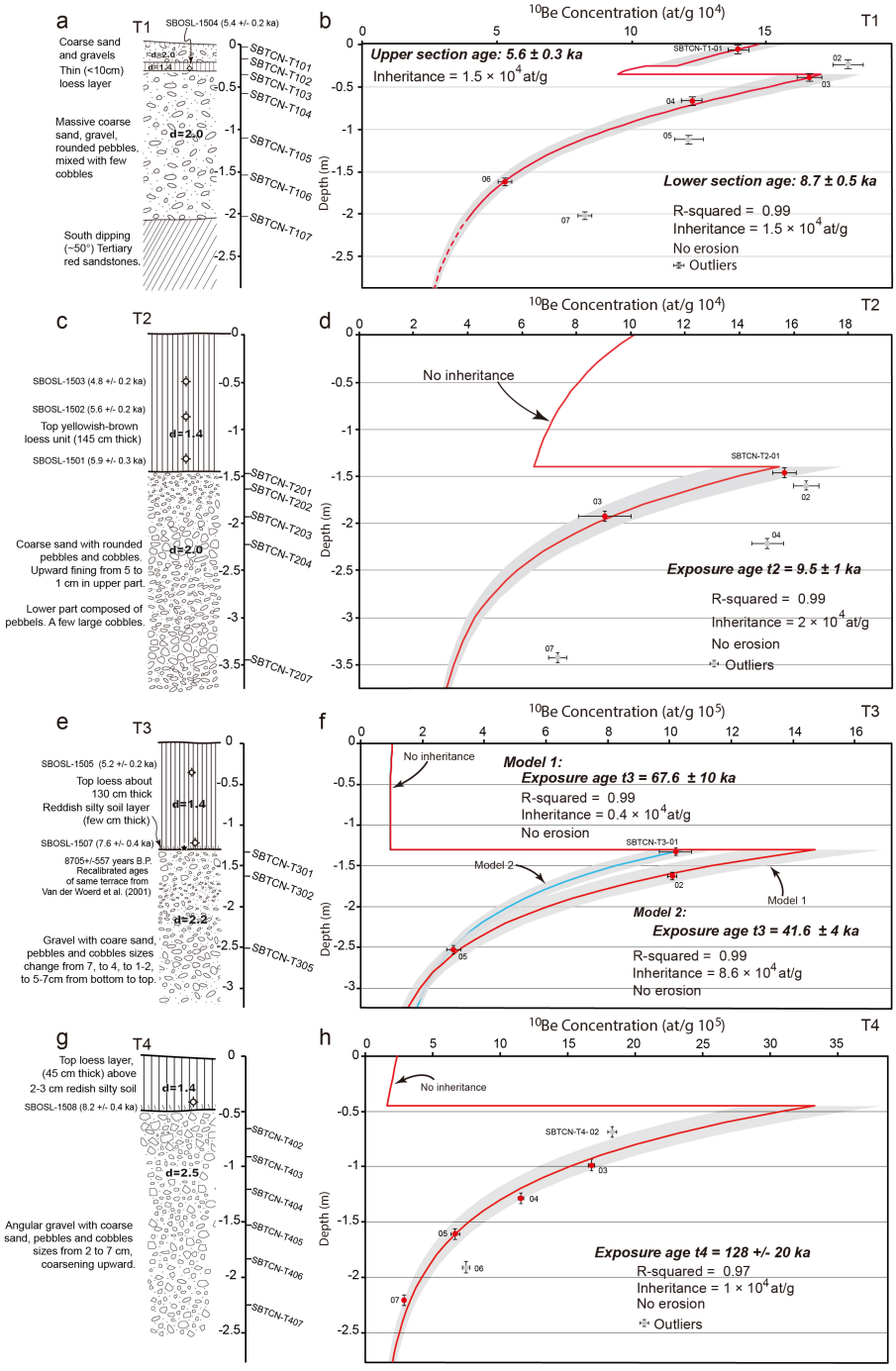

Figure 10. Depth profile description, sample type and position, and ^{10}Be age models for T1, T2, T3, and T4 at site 1. (a), (c), (e), and (g) are simplified stratigraphic logs with sample positions and average layer densities. (b), (d), (f), and (h) are ^{10}Be depth profile models "d" stands for density in g/cm^3. See also alternative models in Figures S3 – S6.

The 3 m-deep depth profile in T3 reveals a ~130 cm-thick loess layer on the top with a thin reddish silty soil layer at its base, indicating weathering and pedogenesis

(Figure 10e). Two OSL samples at depths of ~40 and ~130 cm yield burial ages of 7.6 ± 0.4 ka and 5.2 ± 0.2 ka, respectively (Table 2), indicating loess deposition since ~7.6 ka at a rate of 37 cm/kyr. Three charcoal samples collected ~150 m to the southwest of the depth profile at the conglomerate-loess interface of T3 (see position in Figure 4; van der Woerd et al., 2001) yield consistent maximum ^{14}C AMS ages of 8.2 – 9.2 kyr B.P. for the base of the loess (Table 4). Three conglomerate samples from depths of 1.3 to 2.5 m are used to constrain the exposure age of T3. We suggest two model scenarios that alternatively fit the two top-most samples (Figure 10f). Model 1 treats sample SBTCN-T3-01 as a reworked surface sample, whereas Model 2 treats sample SBTCN-T3-02 as an outlier with larger inheritance. Model 1 yields an exposure age of 67.6 ± 10 ka and Model 2 yields an exposure age of 41.6 ± 4 ka (Figure 10f). In any case, the considerable time lag implied by the TCN modeling (30 to 50 kyr) between the conglomerate deposit and the overlying loess cover indicates that the top terrace remained devoid of loess cover most of its time, consistent with the observation of soil development at its top (Figures 9 and 10e). Given the significant uncertainty, the two models provide the upper and lower bounds on the age of T3 (41 – 68 ka or 51.5 ± 13.5 ka).

The 2.8 m-deep pit in T4 reveals a ~45 cm thick loess layer with a thin reddish silty soil at its base above the terrace conglomerate (Figure 9). One OSL sample at the bottom of the loess yields a burial age of 8.2 ± 0.4 ka (Figure 10g, Table 2). The model yields an exposure age of 128 ± 20 ka by fitting four out of six conglomerate samples (Figure 10h). Samples SBTCN-T4-02 and SBTCN-T4-06 are considred outliers. Sample SBTCN-T4-02 is close to the top of the terrace deposit and may have been bio- or cryo-perturbated. Including sample SBTCN-T4-02 results in a similar age with larger uncertainties (Figure S6). Similar to terrace T3, the time lag between the deposition of the conglomeratic strath and the overlying loess cover (~100 kyr) is consistent with soil development at the top of the conglomerate and indicates no or minimal surface erosion before loess mantled its surface.

At site 2, six embedded granitic boulders from surface Tf2 were targeted for TCN dating (Figure 11). Four (LP02, 03, 04, 06) samples are clustered at approximately 16 ka, with an average age of 16.2 ± 2.5 ka (youngest age of 15.3 ± 1.4 ka) (Table 2; Figure 11). Two samples yielded older dates than the rest of the samples (~25 – 35 ka), probably owing to longer exposure in the catchment upstream resulting in larger inheritance and are thus considered outliers. Since the ages of the four youngest

549 samples are well-clustered, erosion and inheritance may be considered negligible (e.g.,
550 van der Woerd et al., 1998; Ryerson et al., 2006; Matrau et al., 2019). The position of
551 Tf2 relative to the other terrace implies that the date of 16.2 ± 2.5 ka is a maximum
552 emplacement age of the fan surfaces at site 2, indicating that these terraces and fans
553 formed at the end of the last glacial maximum with the return of a more humid
554 climate (e.g., van der Woerd et al., 2002; Hetzel, 2013).

555 In the trench, one radiocarbon sample collected at the bottom of the upper loess
556 unit U1 in the west wall was dated at 8040 – 8190 years B.P.. This age is overall
557 concordant with the base of the loess units at site 1 and even farther west (this study;
558 Tables 2 and 4; see also van der Woerd et al., 2001). When we consider the bottom
559 burial age of the loess covering the terrace conglomerate at ~8 ka, we can bracket the
560 age of Tf2 between 8 and 16.2 ka (12 ± 4 ka).

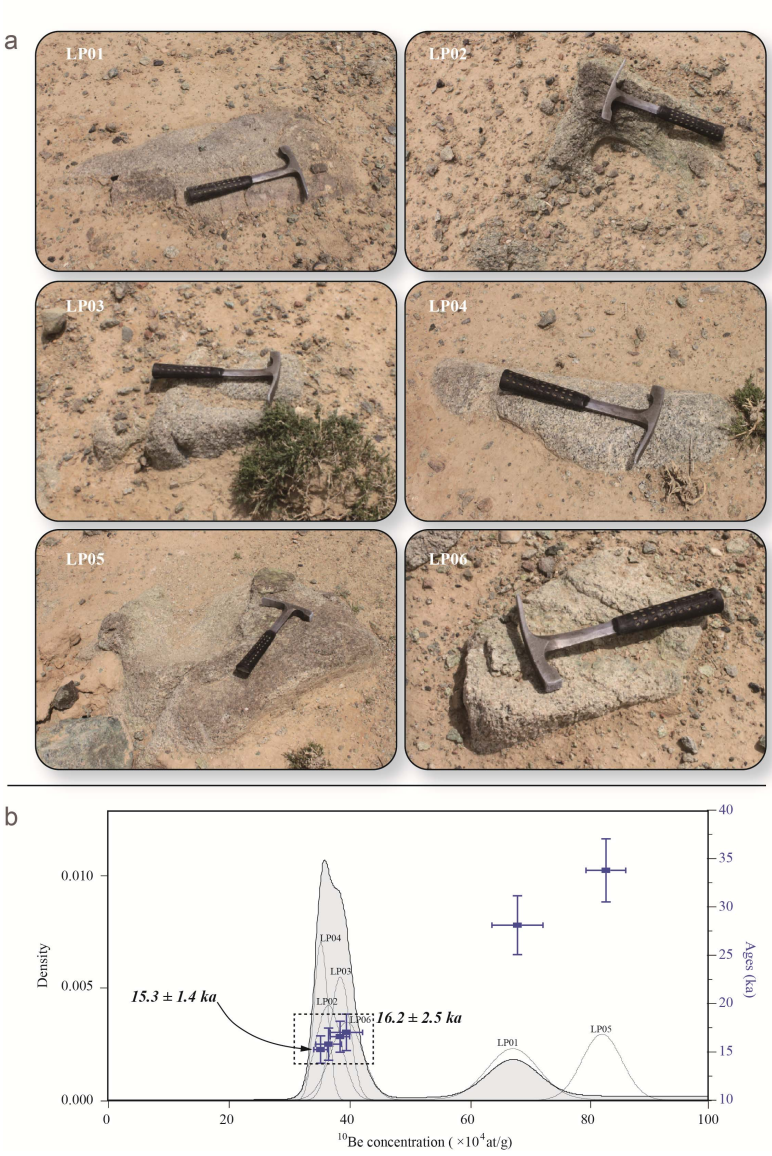

Figure 11. ^{10}Be dating of surface samples at site 2. (a) Samples were collected from the surface of imbedded granitic boulders. Hammer for scale. See Figure 8 and Table 3 for location details. (b) ^{10}Be cosmogenic nuclide concentration and age distributions of TCN samples at site 2 (Table 3). Thin curves are single sample density distribution, and gray shaded area is cumulative density distribution. Four youngest ages cluster with overlapping error bars and constrain alluvial fan (Tf2) abandonment age.

5. Uplift and shortening rates estimates

Site 1 along catchment r5 has been targeted because it is one of the above average sized catchments along the western DHNS range with moderate incision, which has preserved a set of four major terrace levels (Figure 4; e.g., van der Woerd et al., 2001). The tops of terraces T1 to T4 stand 7 to 60 m at their highest point above the present

stream bed (Figure 6). The highest terrace T4, which can be mapped up to the range front, has a slightly steeper slope upstream (7 – 8°) than the present stream bed (6 – 7°), indicating progressing slope lowering with time. In addition, sedimentation at the front of the fold and burial of the older fan deposits also need to be considered when reconstructing older base levels (van der Woerd et al., 2001). Indeed, the present bajada is dominated by deposits related to T2 (see Figure 4), i.e., Holocene fan deposits, and by the present-day active stream outlets and fans that develop farther downslope (Figures 2 and 4; see also van der Woerd et al., 2001). Because the stream gradient changes across the length of the terraces (2° between F0 and F1, i.e., approximately 3 km) and because the past base level geometry is not available, we take the present-day stream bed river profile and its gradient variations as a template for reconstructing past base levels. Given the steeper slope of upstream terrace T4, we thus rotate the present-day stream bed profile to fit the steeper gradient of terrace T4. For terrace T3, we choose an intermediate gradient between that of T4 and the present-day gradient. For T2 and T1, the base level is that of the present-day stream r5 (Figure 12).

The frontal ramp is considered to reach the surface with a dip close to the bedding of the frontal red beds, i.e., approximately 40 – 50° (van der Woerd et al., 2001). The wavelength of the antiformal folding of the terraces averages approximately 1000 m, thus constraining the depth where the ramp and the décollement meet, i.e., at 1000 m depth (D_0; Figures 3 and 12, Table 6). For Model 1, this depth then remains constant until it joins with thrust F0. For Model 2, the décollement dips with an angle α and thus joins F0 at a deeper depth (approximately 1900 m; Figure 12, Table 6).

Shortening results for models 1 and 2 are shown in Table 6. The areas considered are measured between the top present-day folded and uplifted surface of the terraces and the reconstructed base level (Figure 12), neglecting the impact of loess cover and thickness of the conglomerates as their thickness remains small compared to the amounts of incision. Overall, the thickness of the conglomeratic deposit above the strath is approximately 2 – 4 m for T1 and T2 and reaches 5 – 10 m for T3 and T4.

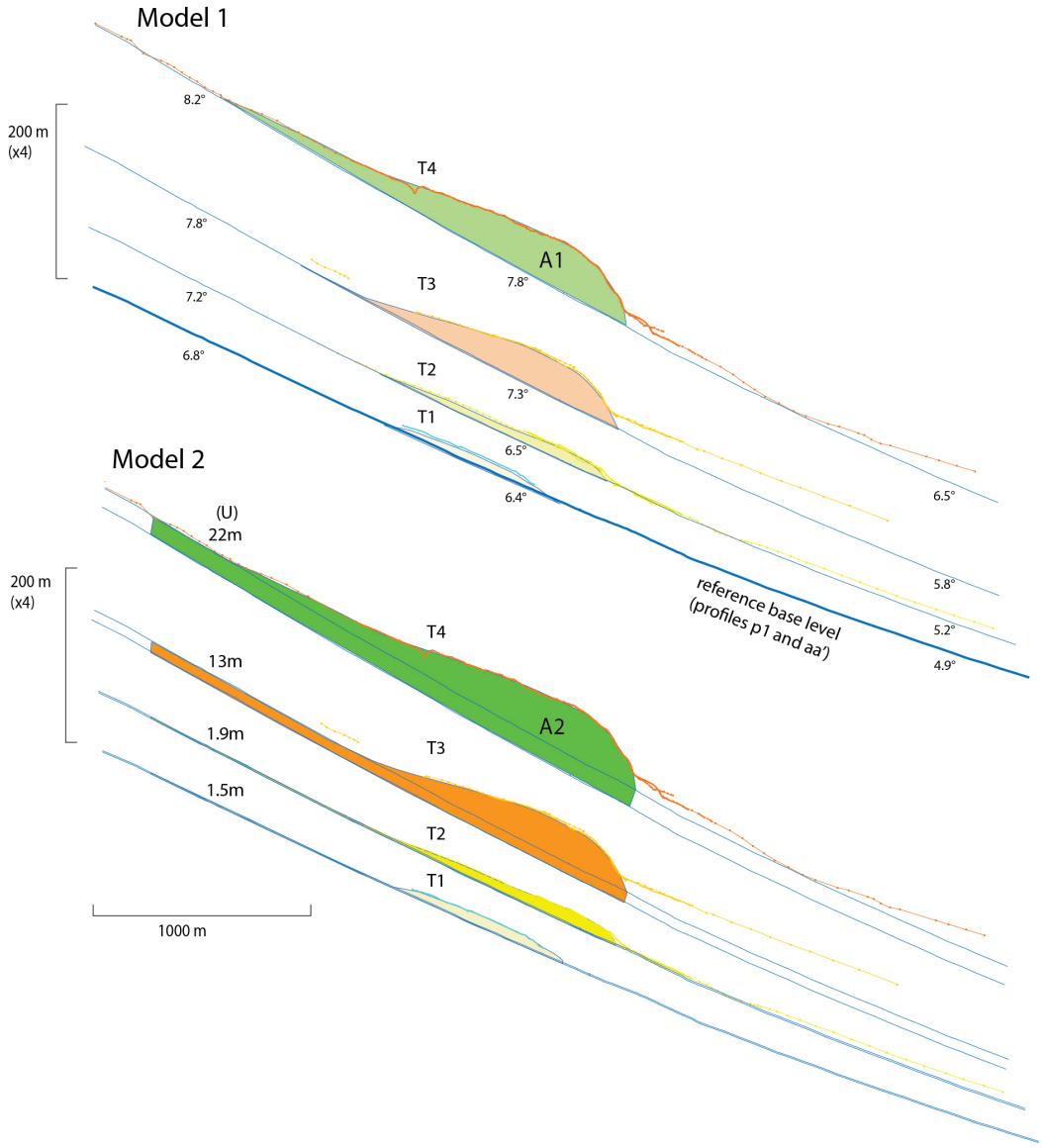

Figure 12. Reconstructed uplifted areas A1 and A2 for the 4 terraces at Site 1 considering end-member models with (Model 2) and without (Model 1) dip of the décollement. Blue lines are reference base levels above which uplifted area is outlined by terrace surface profiles (Figures 4 and 5). See text and Table 6 for details.

In Model 1 shortening is absorbed solely by the warped frontal part of the terraces, and the upstream parts of the terraces are considered to have little or no uplift. The incision of the river is thus driven mainly by progressive base level adjustment (see van der Woerd et al., 2001). For this model, the shortening rate varies from 0.8 – 1.0 mm/yr for T1 and T2 to 0.5 mm/yr for T3 and T4 (Table 6).

Model 2 considers a dipping décollement before it ramps up as fault F1. In this case, shortening is absorbed by both the warped frontal part of the terraces and their uplifted upstream part. The incision of the river is now a combination of both

progressive base level adjustment and overall uplift and folding of the terraces between F0 and F1. With this model, adjusting the dip of the décollement allows to minimize shortening rate differences throughout the set of terraces. An almost constant shortening rate of 0.5 ± 0.1 mm/yr for all terraces can be calculated with a dip of 23.5°, the corresponding uplift rate is 1.1 ± 0.3 mm/yr (Table 6).

At site 2, the 4.9 ± 0.5 m total slip on all branches of fault F2, as revealed from trenching may correspond to slip on a 47° dipping ramp to account for the 3.6 ± 0.2 m cumulative uplift and approximately 3.4 ± 0.2 m of shortening of Tf2. Dividing the slip values by the age of Tf2 (12 ± 4 ka) yields uplift and shortening rates of 0.5 ± 0.1 mm/yr on fault F2.

Considering the less well constrained shortening rate along thrust F2, and accounting for some shortening accommodated along thrust F0, total uplift and shortening rates along the western Danghe Nan Shan range front, south of Subei, for the last 130 ka could reach 1.4 ± 0.4 mm/yr and 0.8 ± 0.2 mm/yr, respectively.

6. Discussion

6.1. Shortening rate bias due to unsteady base level

Using terrace heights in the hanging wall of active thrusts to estimate shortening rate requires knowledge of a reference base level (e.g., Merrits et al., 1994; Guilbaud et al., 2017; Hetzel et al., 2004; Lavé & Avouac, 2000; van der Woerd et al., 2001; Daeron et al, 2007; Hu et al., 2021). Although changes with time of the base level are almost always a dynamic adjustment to the sediment supply or the transport capacities of a stream, they can be triggered by various causes, such as climate change, stream capture, subsidence, uplift, and earthquake-triggered changes in sediment supply (Tapponnier et al., 1990; Merrits et al., 1994; van der Woerd et al., 2002; Bull, 2008; Poisson & Avouac, 2004; Rizza et al., 2019). Long-term tectonic uplift is a cause of changes in base level when erosion and incision are not able to compensate for uplift. This is the situation along the western DHNS range front, where small and steep catchments are uplifted (van der Woerd et al., 2001). As a consequence, aggradation occurs in the bajada south of Subei, as shown by the youth of the fan deposits (fan Tf2 of Holocene age) burying older deposits.

We have no subsurface data of the deposits in the footwall of fault F1. However, according to our mapping (Figure 3), fan Tf2 deposits in the footwall correspond to terrace T2 in the hanging wall, which indicates that the pre-Holocene corresponding

footwall terrace deposits are buried. This is considered in Model 2 (Figure 12). Therefore, the heights of terraces T3 and T4 above their respective base levels are possibly greater than 13 and 22 m, as suggested in Model 2 (Figure 12; Table 6). Consequently, the estimated shortening is minimized.

6.2. Shortening model implementation

Contrary to large mountains belt incised by large rivers (>50 km long), like in the North Qilian Shan, the Western Kunlun Shan, the Tian Shan, the catchment lengths west of Subei barely exceed about 5 km. As a consequence, the intermittent streams that incise the western DHNS are far from being stabilized graded rivers over long time periods. Shortening models as proposed, for instance, by Hu et al. (2015), Thompson et al. (2002), are well adapted for the development of folds along stable rivers with almost no large base level changes and negligible slope changes. This is not the case west of Subei, where, as explained above, we still fail to reconstruct a reliable base level throughout the deposition time span (130 ka) of all the terraces. We thus choose to adapt our simplified structural model to this situation by considering two end-members, one without dipping décollement (Model 1) and another with a dipping décollement (Model 2) (Figure 3). Both situations are equally possible as illustrated by the variety of well documented fold and thrust belts across central Asia (e.g., Tapponnier et al., 1990; Avouac and Tapponnier, 1993; Meyer et al., 1998; van der Woerd, 1998; van der Woerd et al., 2001; Poisson and Avouac, 2004; Hubert-Ferrari et al., 2007; Guilbaud et al., 2017).

Making the right assumptions for assigning parameters to estimate shortening rate is challenging (Figure 3; see also, for instance, Suppe and Medwedeff, 1990; Lave and Avouac, 2000; Thompson et al., 2002; Hu et al., 2015). Here, we use the topographic profiles (Figure 5) and ages (Figure 10) of 4 incrementally folded terraces together with both a changing base level with time (slope decrease) and a changing décollement dip (from flat to dipping) (Figures 3 and 12). The 2 proposed end-member models capture a large range of the variability in shortening rate estimates (0.4 to 1 mm/yr, Table 6) although, as explained above, these rates might still be minimum rates (Figures 2, 13, 14).

6.3. Link with long-term cumulative shortening and exhumation

Accelerated range growth between 13.7 Ma and 9 Ma inferred from magnetostratigraphy (Sun et al., 2005) is correlated with the deposition of coarse conglomerate deposits along Tiejangou (see location in Figure 2). Provenance change

686 and lag-time variation of detrital apatite fission-track data in the same section
687 corroborate a tectonic pulse at 14 Ma (Lin et al., 2015). Consistently, apatite fission-
688 track and apatite (U-Th)/He data from three bedrock transects in the western DHNS
689 (see location in Figure 2) suggest a period of rapid exhumation of approximately 0.1
690 to 0.3 mm/yr from 16 to 9 Ma (Yu et al., 2019).

691 Balanced geological sections indicate cumulative shortening of 10 – 20 km by
692 thrusts F0 and F1, based on structural constraints along several river cuts with an
693 onset of shortening likely at 9 – 14 Ma based on the age of the uppermost coarse
694 conglomerate (Gilder et al., 2001; van der Woerd et al., 2001). The average
695 shortening rate is thus estimated at 1.5 ± 0.7 mm/yr since the late Miocene. This
696 estimate may indicate a near-constant shortening rate since 14 Ma when compared to
697 our late Pleistocene rate. In addition, it indicates that F1 and F2 accommodate most of
698 the shortening responsible for the present-day uplift of the western DHNS.
699 Conversely, it may suggest that F0 or the southern DHNS thrust do not accommodate
700 much shortening, although more work is probably needed on these mostly bedrock
701 faults to assess their slip history.

702 6.4. Slip accommodation at the Subei junction: geometric and kinematic 3D
703 complexities

704 *6.4.1 The fault geometry in 3D*

705 The Subei junction is particularly complex and involves numerous active faults,
706 including strike-slip faults, thrusts, and normal faults (e.g., Meyer et al., 1998). The
707 N70°E striking north strand of the ATF (NATF) connects the Aksay section with the
708 Shibao Cheng section to the northeast (Figure 1). West of Subei, the N135°E-striking
709 and south-dipping thrusts of the western DHNS veer to the west and connect with the
710 NATF. Although the NATF can be traced continuously, thrusting also occurs north of
711 it but west of the junction (e.g., van der Woerd et al., 2001). East of the junction and
712 north of NATF, normal faults run parallel to the ATF for 20 km across the Subei
713 basin and Dang He (Figures 2 and S2). Slip transfer from NATF to the DHNS, and
714 rigid block kinematics explain the extensional component northeast of the junction
715 (e.g., Meyer et al., 1998). In the long term, these kinematic interactions also explain
716 the long-lived Subei trough along the NATF.

717 The geological and topographical continuity of the arcuate shape of the western
718 DHNS range, underlined by the continuous trace of the south strand of the ATF
719 (SATF), testifies to the time-progressive accumulation of deformation both by strike-

slip faulting along the ATF and shortening across the DHNS range. This long-term coupling of strike-slip faulting and thrusting accommodated the strain at the margin of the Tibet plateau contributing to continental plateau growth and widening (e.g., Meyer et al., 1998; Tapponnier et al., 2001; van der Woerd, 1998; van der Woerd et al., 2001). The two sub-parallel, arcuate ranges of Guai Zhang Shan (GZS) and DHNS, with their contrasted morphology, further depict this long-term coupling. GZS summits are only slightly below the peaks of DHNS, although it is not bounded by active thrust faults. On the contrary, valleys and mountain slopes merge gently with the surrounding sedimentary basin fills, indicating no tectonic activity but passive erosion. We thus infer that GZS grew in the early Miocene and stopped growing as strain stepped northeastward along the ATF (Figure 12). Describing the full 3D geometry of the Subei junction is beyond the scope of this study, and we only stress part of this complexity to address the difficulty of balancing the kinematics across the junction.

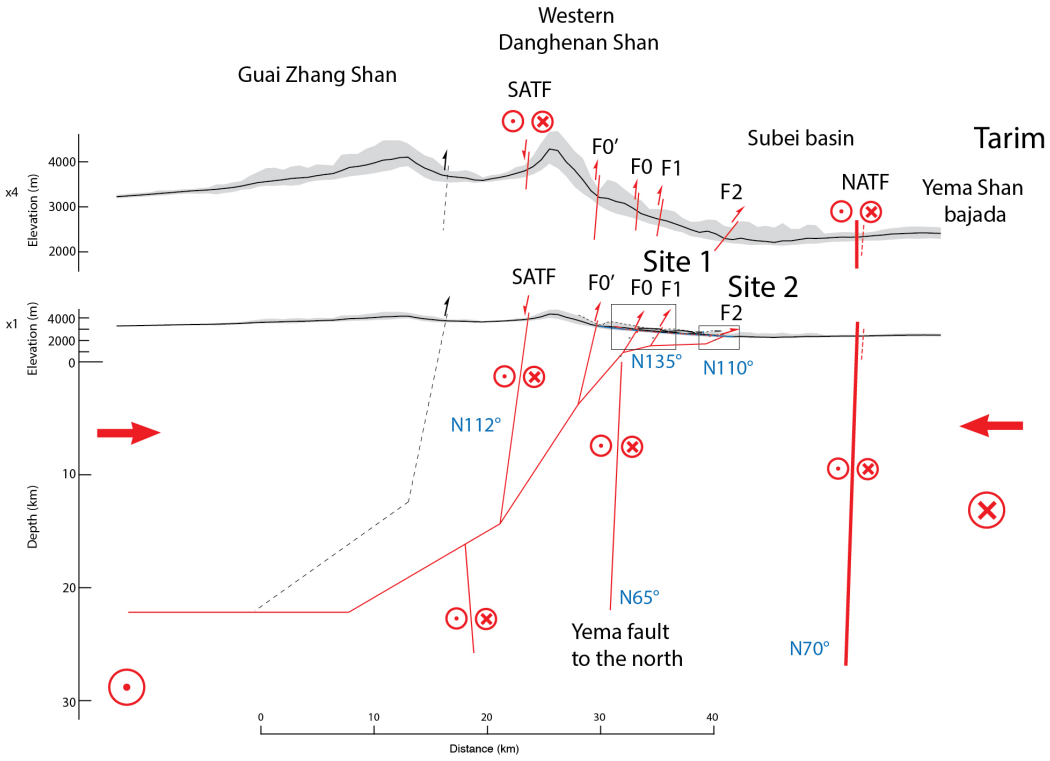

Figure 13. Simplified tectonic section across western Danghe Nan Shan with possible fault geometry at depth (see location of faults and section in Figures 1 and 2). Thrust fault north of Guai Zhang Shan (black dashed line) is inferred. Blue labels present fault strikes.

Although the structural link in map view is clear between the thrusts F0', F0 and F1 with the N70°E striking ATF, how thrusts faults that root onto shallow dipping ramps and décollement at the crustal level (e.g., Meyer et al., 1998) are linked with subvertical lithospheric scale strike-slip fault (e.g., Wittlinger et al., 2004) is not straightforward. Our mapping (Figures 1 and 2) and section (Figure 13) suggest a transition from strike-slip to thrusting as faults progressively deviate from the N70°E direction of the main ATF and become perpendicular to the main stress direction (N45°E) as depicted in thrust focal mechanisms (Figure 1) or the average geodetic displacement field direction (Wang and Shen, 2020). Southeast of Subei, other strike-slip faults emerge (YDS or YNS) at the eastern fold tip implying kinematic links and slip transfer from thrusting to strike-slip faulting (Figures 2, 13 and 14).

6.4.2 Slip accommodation by the western Danghe Nan Shan

If the amount of shortening along the DHNS results entirely from slip transfer from the north strand of ATF, then a similar amount of left-slip rate is lost for the north strand of ATF eastward from the Subei junction. Our estimated shortening rate on fault F1 is approximately 0.5 mm/yr (Table 6), and the total, including fault F2 and possible additional slip on F0, could amount to 1 mm/yr. There is no doubt that the rate of slip of the north strand of the ATF decreases toward the east (e.g., Xu et al., 2005; Wang and Shen, 2020; Xu. et al., 2021; Figure S2), however, where and how the slip is distributed remains difficult to constrain.

If all the left-slip displacement along the ATF is absorbed in the Qilian Shan region in shortening or left-lateral faulting (Tapponnier and Molnar, 1977; Peltzer et al., 1989; Burchfiel et al., 1989; Meyer et al., 1998; Tapponnier et al. 2001) and the knowledge of slip rate on each fault is known, one should be able to build an equilibrated kinematic budget between slip on the ATF and the other faults to the southeast (Figure 14). However, slip rates on faults are variably documented in the Qilian Shan region (Figure S2, Table S1).

Figure 14 suggests an overall slip-rate decrease along ATF from about 10 mm/yr west of Aksay to a few mm/yr east of the Qilian Shan junction at 97°E. At the Subei junction, our shortening rates and published rates on adjacent faults may point to kinematic incompatibilities. On one hand (Figure 14a), if indeed YDS and YNS faults connect southeast of thrusts F1 and F2, our maximum total shortening of 1 mm/yr is low compared to the published rates on YDS (2 – 3 mm/yr; Luo et al., 2015) and YNS

(3 mm/yr; Zheng et al., 2013), as well as shortening along DXS (1-3 mm/yr; Meyer et al., 1998; Luo et al., 2015) (Figure 14a). The rates on YDS and YNS may suggest additional connection to the ATF in addition to thrust F1 and F2, which might be found in thrust faults within the western DHNS, mapped as faults F0' and F0 (Figures 2 and 13). Thrusts faults F0' and F0 cut through western DHNS bedrock and may have been overlooked. On the other hand (Figure 14b), rates along YDS and YNS may be overestimated and no additional slip transfer from faults F1 and F2 is needed. In this case, the ATF slip-rate east of Subei remains larger and more slip is transferred in the junctions eastward, at Shibao Cheng/Changma and Qilian (Figures 1 and 14).

Complex fault systems are subject to slip variations as faults interact in time and space during their seismic cycle (e.g., Dolan et al., 2016; Matrau et al., 2019; Bennet et al., 2004). Building a kinematic budget as proposed in Figure 14 implies that rates are known over similar temporal periods or that their rates remain constant over long-time scale. Very few rates are determined for time scales larger than the last 10 ka (Table S1). Knowing that the return time of large magnitude 7 – 8 earthquake in the region is on the order of a few 1000 years (Figure 1; e.g., Luo et al., 2019), makes these rates highly dependent on their seismic cycle. Discussing variations in slip-rate in space and time, even along the ATF that is the most documented fault in the area, remains challenging.

Overall, the rate we found along the western DHNS near Subei is comparable to the rate estimated eastward along the same range in Yanchi Wan (Figure 1; Xu et al., 2021). It is also comparable to other rates along the northern Qilian Shan using similar approaches (e.g., Tapponnier et al., 1990; Hetzel et al., 2004; Hu et al., 2015; Yang et al., 2018; Wang et al., 2020), which indicates that the NE-SW directed shortening in the DHNS, together with other thrust faults, contributes to overall crustal shortening in the Qilian Shan region.

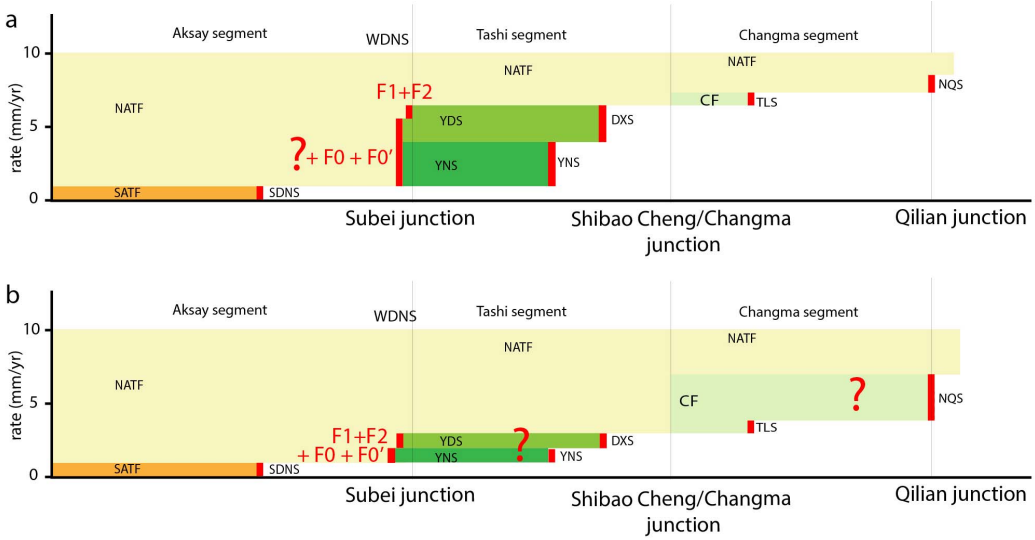

Figure 14. Schematic kinematic budget along ATF (see Figure S2, and Table S1). Width of color band is rate. Red bars are shortening rates connected to strike-slip faults. (a) Published rates on YDS and YNS are larger than our determined rates on F1 and F2. Possibly, rates of F0 and F0' are underestimated. (b) Rates on YDS and YNS are overestimated as well as the shortening rates along DXS and YNS. Strike-slip rate is larger on ATF east of Subei, and shortening rates larger on TLS and QS. NATF: north strand of Altyn Tagh fault, SATF: south strand of Altyn Tagh fault, SDNS: south Danghe Nan Shan thrust, WDNS: western Danghe Nan Shan thrust, CF: Changma fault, TLS: Tuolai Shan thrust, NQS: Northern Qilian Shan thrust, DXS: Daxue Shan thrust, YNS: Yema Nan Shan thrust.

6.5. Seismic hazards

Evaluating seismic hazards in the Subei area becomes critical due to population growth and the new traffic line across the Danghe Nan Shan thrust and the Altyn Tagh fault (Figure 2). There is no historical record of large earthquakes in the Subei basin related to faulting along the northern DHNS thrust. However, multiple 0.6 to 2.7 m-high fault scarps across the fans in front of the frontal folded hills (e.g., site 3 of van der Woerd et al., 2001; site 2 of this study; Figure 2) suggest several surface rupturing events in the Holocene. A paleoseismic trench across one of these scarps on a lower terrace by Wu et al. (2017) shows evidence of slip on a 20 – 25° dipping fault plane and ~1.7 m vertical offset after ~4.2 ka B.P. The ~1.5 m high scarp across the same terrace has been suggested to result from one seismic event, while the 2.6 – 3.3 m cumulative vertical offset of this terrace, approximately twice the height of the scarp, implies a record of two earthquakes (van der Woerd et al., 2001). Although no evidence of a penultimate event was described in the trench (Wu et al., 2017), we cannot rule out the possibility of the occurrence of one older event in the frontal ramp

and folding in the hanging wall.

At site 2, similar 1.5 – 3.6 m scarp heights are observed across various terraces (Figures 5, 6). The young terraces (pf2 and pf3) show smaller offsets (1.5 m) than the older terraces (pf4-pf5 with offsets up to 3.5 – 3.6 m), suggesting the occurrence of two events, with the latest event occurring after emplacement of the youngest terrace. The ages of these two events are loosely constrained by limiting ages at site 2. In the trench, a radiocarbon sample under the younger event horizon provides an age of 8.1 ka for the loess unit (U1). The exposure age of the terrace defines a maximum age of 16.2 for the gravels unit (U2). We then can bracket the occurrence time of the older event between 16.2 and 8.1 ka and the younger event after 8.1 ka. According to the ages of these events, it is possible that the younger event at site 2 correlates with the recent event at site 3.

Earthquake magnitude can be estimated by the empirical relationship of rupture parameters (e.g., Wells & Coppersmith, 1994). There is no strong evidence indicating that sites 2 and 3 (15 km apart) along two different structures (F1 and F2) have ruptured together during the same seismic events. The sizes of the minimum slip events at both sites, however, are compatible with concomitant 20 km-long ruptures. It is thus tempting to suggest a minimum magnitude of 6.5 – 7 (1 – 2 m of slip over 20 km).

We suggest that both thrusts F1 and F2 merge into one ramp and décollement at depth (Figure 13). Mapping of the surface trace of the thrusts and the deformed terraces and fans in their hanging wall constrain in part the geometry of the ramp and décollement at depth (e.g., Meyer et al., 1998; Stockmeyer et al., 2014). The combination of co-seismic thrust scarp measurements and the cumulative deformation of the thrusts makes it possible to suggest the occurrence of events with multi-fault ruptures. Taking the length of the thrust system (20 km), the total width of the ramps and décollement above a depth of 15 km (20 km), and a total slip at depth of 4 m distributed on F1 and F2 would result in a seismic moment of 7.9×10^{19} N.m with the shear modulus of 3.3×10^{10}N/m$^{-2.}$ Such a moment is compatible with a moment magnitude of Mw=7.2 (e.g., Kanamori, 1977).

Complex ruptures on multiple faults are not uncommon, as described above. In Subei, thrust faults F1 and F2 are connected with strike-slip faults to the west and to the east (see Figures 2 and S2). These connected faults could rupture together similarly to the 2016 Mw7.8 Kaikōura complex earthquake rupture (e.g., Klinger et

al., 2018). Previous paleoseimic investigations show that temporally consistent events ruptured on these faults (Xu et al., 2007; He et al., 2018; Luo et al., 2019). For instance, both the Subei-Old Aksay section of the north strand of Altyn Tagh fault, the Yema-Daxue Shan fault ruptured in 6.3 – 6.8 ka (Xu et al., 2007; He et al., 2018), and the east section (east of Subei) of the north strand of Altyn Tagh fault also ruptured in 6.4 – 7.2 ka (Luo et al., 2019). The section from Old Aksay to Shibao Cheng of the north strand of Altyn Tagh fault ruptured in 2.6 – 2.8 ka, which is consistent with the most recent event of the Danghe Nan Shan thrust. While the date uncertainties may only indicate close in time ruptures, it is not possible to rule out simultaneous ruptures on several faults. Thus, if combined ruptures involving both the thrust system and strike-slip faults are considered, then our magnitude estimation above is a minimum. One such earthquake could potentially damage local infrastructure. More structural and paleoseismic investigations involving all the active faults, are needed to assess the seismic hazard of the complex fault system in and around the Subei basin.

7. Conclusion

Based on field investigations and high-accuracy topographic surveys of multiple folded terraces along the western DHNS, we constrain the cumulative and recent activity of two thrusts. Considering 2D mass balance across the fold and thrust belt, with either a flat décollement or a dipping décollement allows us to constrain the amount of accumulated shortening. Integrating the terrace ages constrained by cosmogenic nuclides, OSL, and ^{14}C dating methods, we estimate a minimum shortening rate of 0.8 ± 0.2 mm/yr for the northern thrusts of the western DHNS for the last 130 ka. This rate is also compatible with the long-term shortening estimate, which implies that the shortening rate across the DHNS has remained constant since the upper Miocene. Our results indicate that the NE-SW-directed shortening along the western DHNS thrusts contributes to slip-rate decrease along the main ATF and slip-transfer to other thrust and strike-slip faults to the east. Evidence of surface seismic ruptures and large earthquakes is clear from scarps and trenches along the western DHNS. We suggest the possible occurrence of Mw7+ earthquake southwest of Subei. Considering the structural links between the thrust system of the western DHNS and the strike-slip faults of ATF to the northwest or Yema-Daxue Shan to the southeast, earthquake ruptures may involve both strike-slip and thrust faults allowing for larger magnitude events.

Data Availability Statement

The historical earthquakes are from the China Earthquake Data Center (CEDC, http://data.earthquake.cn/index.html). The raw datasets of DEM derived from satellite images (https://doi.org/10.5281/zenodo.7045176) and LiDAR point cloud (https://doi.org/10.5281/zenodo.7045169) are shared in zenodo.org, and as well as the terrace survey data of site 1 (https://doi.org/10.5281/zenodo.7070457). The focal mechanisms come from the Global Centroid Moment Tensor project (CMT; http://www. globalcmt.org).

Acknowledgments

This work is jointly funded by the National Key Research and Development Program of China (2017YFC1500100), the Second Tibetan Plateau Scientific Expedition and Research Program (STEP) (2019QZKK0901), and the National Natural Science Foundation of China (41802228, U1839203), the Basic Research Project of Lanzhou Institute of Seismology (2018IESLZ01). YS has been partly supported by a grant from K.C. Wong Foundation and CNRS. We thank ASTER Team (D. Bourlès, G. Aumaître, Vincent Godard, Régis Braucher and K. Keddadouche) at ASTER-CEREGE for ^{10}Be AMS measurements. ASTER AMS national facility (CEREGE, Aix-en-Provence, France) is supported by INSU/CNRS, ANR through "Projets thématiques d'excellence" program for "Equipements d'excellence" ASTER-CEREGE action, and IRD.

References

Anderson, R. S., Repka, J. L., & Dick, G. S. (1996). Explicit treatment of inheritance in dating depositional surfaces using in situ 10Be and 26Al. Geology, 24(1), 47–51. https://doi.org/10.1130/0091-7613(1996)024

Avouac, J. P., Tapponnier, P., Bai, M., You, H., & Wang, G. (1993). Active thrusting and folding along the northern Tien Shan and late Cenozoic rotation of the Tarim relative to Dzungaria and Kazakhstan. Journal of Geophysical Research: Solid Earth, 98(B4), 6755-6804.

Balco, G., Stone, J. O., Lifton, N. A., & Dunai, T. J. (2008). A complete and easily accessible means of calculating surface exposure ages or erosion rates from 10Be and 26Al measurements. *Quaternary Geochronology*, *3*(3), 174–195.

https://doi.org/10.1016/j.quageo.2007.12.001

Bemis, S. P., Micklethwaite, S., Turner, D., James, M. R., Akciz, S., Thiele, S. T., & Bangash, H. A. (2014). Ground-based and UAV-Based photogrammetry: A multi-scale, high-resolution mapping tool for structural geology and paleoseismology. *Journal of Structural Geology*, *69*, 163–178. https://doi.org/10.1016/j.jsg.2014.10.007

Borchers, B., Marrero, S., Balco, G., Caffee, M., Goehring, B., Lifton, N., Nishiizumi, K., Phillips, F., Schaefer, J., Stone, J. (2016). Geological calibration of spallation production rates in the CRONUS-Earth project. Quat. Geochronol. 31, 188-198.

Braucher, R., Brown, E. T., Bourlès, D. L., & Colin, F. (2003). In situ produced 10Be measurements at great depths: implications for production rates by fast muons. *Earth and Planetary Science Letters*, *211*(3), 251–258. https://doi.org/10.1016/S0012-821X(03)00205-X

Bull, W.B. (1991). *Geomorphic responses to climatic change*. Oxford University Press, Oxford.

Bull, W. B. (2008). *Tectonic geomorphology of mountains: a new approach to paleoseismology*. John Wiley & Sons.

Burchfiel, B. C., Quidong, D., Molnar, P., Royden, L., Yipeng, W., Peizhen, Z., & Weiqi, Z. (1989). Intracrustal detachment within zones of continental deformation. *Geology*, *17*(8), 748–752. https://doi.org/10.1130/0091-7613(1989)017<0448:IDWZOC>2.3.CO;2

Bureau of Geology and Mineral Resources of Gansu Province, (1989). Regional Geology of Gansu Province. Geological Publishing House, Beijing (in Chinese)

Daëron, M., Avouac, J. P., & Charreau, J. (2007). Modeling the shortening history of a fault tip fold using structural and geomorphic records of deformation. Journal of

955 Geophysical Research: Solid Earth, 112(B3).
956 https://doi.org/10.1029/2006JB004460
957 Dai, S., Fang, X., Dupont-Nivet, G., Song, C., Gao, J., Krijgsman, W., et al. (2006).
958 Magnetostratigraphy of Cenozoic sediments from the Xining Basin: Tectonic
959 implications for the northeastern Tibetan Plateau. *Journal of Geophysical*
960 *Research: Solid Earth*, *111*(B11). https://doi.org/10.1029/2005JB004187
961 Dolan, J.F., L.J. McAuliffe, E. J. Rhodes, S.F. McGill, R. Zinke (2016). Extreme
962 multi-millennial slip rate variations on the Garlock fault, California: Strain super-
963 cycles, potentially time-variable fault strength, and implications for system-level
964 earthquake occurrence. Earth and Planetary Science Letters, 446, 123-136.
965 http://dx.doi.org/10.1016/j.epsl.2016.04.011
966 Du, J., Fu, B., Guo, Q., Shi, P., Xue, G., & Xu, H. (2020). Segmentation and
967 termination of the surface rupture zone produced by the 1932 Ms 7.6 Changma
968 earthquake: New insights into the slip partitioning of the eastern Altyn Tagh fault
969 system. *Lithosphere*, *12*(1), 19–39. https://doi.org/10.1130/L1113.1
970 Dupont-Nivet, G., Horton, B. K., Butler, R. F., Wang, J., Zhou, J., & Waanders, G. L.
971 (2004). Paleogene clockwise tectonic rotation of the Xining-Lanzhou region,
972 northeastern Tibetan Plateau. *Journal of Geophysical Research: Solid Earth*,
973 *109*(B4). https://doi.org/10.1029/2003JB002620
974 Elliott, A. J., Oskin, M. E., Liu-zeng, J., & Shao, Y.-X. (2018). Persistent rupture
975 terminations at a restraining bend from slip rates on the eastern Altyn Tagh fault.
976 Tectonophysics, 733, 57–72. https://doi.org/10.1016/j.tecto.2018.01.004
977 Gaudemer, Y., Tapponnier, P., Meyer, B., Peltzer, G., Shunmin, G., Zhitai, C., et al.
978 (1995). Partitioning of crustal slip between linked, active faults in the eastern
979 Qilian Shan, and evidence for a major seismic gap, the 'Tianzhu gap', on the

western Haiyuan Fault, Gansu (China). Geophysical Journal International, 120(3), 599-645.

George, A. D., Marshallsea, S. J., Wyrwoll, K.-H., Jie, C., & Yanchou, L. (2001). Miocene cooling in the northern Qilian Shan, northeastern margin of the Tibetan Plateau, revealed by apatite fission-track and vitrinite-reflectance analysis. *Geology*, *29*(10), 939–942. https://doi.org/10.1130/0091-7613(2001)029<0939:MCITNQ>2.0.CO;2

Gilder, S., Chen, Y., & Sen, S. (2001). Oligo-Miocene magnetostratigraphy and rock magnetism of the Xishuigou section, Subei (Gansu Province, western China) and implications for shallow inclinations in central Asia. *Journal of Geophysical Research: Solid Earth*, *106*(B12), 30505–30521. https://doi.org/10.1029/2001JB000325

Gosse, J. C., & Phillips, F. M. (2001). Terrestrial in situ cosmogenic nuclides: theory and application. *Quaternary Science Reviews*, *20*(14), 1475–1560. https://doi.org/10.1016/S0277-3791(00)00171-2

Guilbaud, C., Simoes, M., Barrier, L., Laborde, A., Van der Woerd, J., Li, H., et al. (2017). Kinematics of active deformation across the western Kunlun mountain range (Xinjiang, China) and potential seismic hazards within the southern Tarim basin. *Journal of Geophysical Research: Solid Earth*, *122*(12), 10–398.

Guo, P., Han, Z., Gao, F., Zhu, C., & Gai, H. (2020). A new tectonic model for the 1927 M8. 0 Gulang earthquake on the NE Tibetan Plateau. Tectonics, 39(9), e2020TC006064.

Hancock, G. S., Anderson, R. S., Chadwick, O. A., & Finkel, R. C. (1999). Dating fluvial terraces with 10Be and 26Al profiles: Application to the Wind River, Wyoming. Geomorphology, 27(1-2), 41-60.

1005 He Wen-gui, Zhang Bo, Wu Ming, Wang Peng-tao, Zou Xiao-bo, Gao Xiao-dong.
1006 (2018). Paleoseismology on the Yemahe segment of the Yemahe-Daxueshan fault
1007 revealed by trench study. Seismology and Geology, 40(1): 261-275.
1008 Hetzel, R. (2013). Active faulting, mountain growth, and erosion at the margins of the
1009 Tibetan Plateau constrained by in situ-produced cosmogenic nuclides.
1010 *Tectonophysics*, *582*, 1–24. https://doi.org/10.1016/j.tecto.2012.10.027
1011 Hetzel, R., Tao, M., Stokes, S., Niedermann, S., Ivy-Ochs, S., Gao, B., et al. (2004,
1012 December 1). Late Pleistocene/Holocene slip rate of the Zhangye thrust (Qilian
1013 Shan, China) and implications for the active growth of the northeastern Tibetan
1014 Plateau. https://doi.org/10.1029/2004TC001653
1015 Hetzel, R., Hampel, A., Gebbeken, P., Xu, Q., & Gold, R. D. (2019). A constant slip
1016 rate for the western Qilian Shan frontal thrust during the last 200 ka consistent
1017 with GPS-derived and geological shortening rates. *Earth and Planetary Science*
1018 *Letters*, *509*, 100–113. https://doi.org/10.1016/j.epsl.2018.12.032
1019 Horton, B. K., Dupont-Nivet, G., Zhou, J., Waanders, G. L., Butler, R. F., & Wang, J.
1020 (2004). Mesozoic-Cenozoic evolution of the Xining-Minhe and Dangchang
1021 basins, northeastern Tibetan Plateau: Magnetostratigraphic and biostratigraphic
1022 results. *Journal of Geophysical Research: Solid Earth*, *109*(B4).
1023 https://doi.org/10.1029/2003JB002913
1024 Hu, X., Pan, B., Kirby, E., Gao, H., Hu, Z., Cao, B., et al. (2015). Rates and
1025 kinematics of active shortening along the eastern Qilian Shan, China, inferred
1026 from deformed fluvial terraces. Tectonics, 34(12), 2478-2493.
1027 Hu, X., Cao, X., Li, T., Mao, J., Zhang, J., He, X., et al. (2021). Late Quaternary Fault
1028 Slip Rate Within the Qilian Orogen, Insight Into the Deformation Kinematics for
1029 the NE Tibetan Plateau. Tectonics, 40(5), e2020TC006586.

https://doi.org/10.1029/2020TC006586

Hu, Z., Yang, X., Yang, H., Huang, W., Wu, G., Miao, S., & Zhang, L. (2021). Slip Rate and Paleoseismology of the Bolokenu-Aqikekuduk (Dzhungarian) Right-Lateral Strike-Slip Fault in the Northern Tian Shan, NW China. *Tectonics*, *40*(8), e2020TC006604. https://doi.org/10.1029/2020TC006604

Hubbard, J., Shaw, J. H., & Klinger, Y. (2010). Structural Setting of the 2008 Mw 7.9 Wenchuan, China, EarthquakeStructural Setting of the 2008 Mw 7.9 Wenchuan, China, Earthquake. Bulletin of the Seismological Society of America, 100(5B), 2713-2735.

Hubbard, J., Almeida, R., Foster, A., Sapkota, S. N., Bürgi, P., & Tapponnier, P. (2016). Structural segmentation controlled the 2015 Mw 7.8 Gorkha earthquake rupture in Nepal. Geology, 44(8), 639-642.

Hubert-Ferrari, A., Suppe, J., Gonzalez‐Mieres, R., & Wang, X. (2007). Mechanisms of active folding of the landscape (southern Tian Shan, China). Journal of Geophysical Research: Solid Earth, 112(B3). https://doi.org/10.1029/2006JB004362

Kanamori, H. (1977). The energy release in great earthquakes. Journal of geophysical research, 82(20), 2981-2987.

Klinger, Y., Xu, X., Tapponnier, P., Van der Woerd, J., Lasserre, C., & King, G. (2005). High-resolution satellite imagery mapping of the surface rupture and slip distribution of the M w~ 7.8, 14 November 2001 Kokoxili earthquake, Kunlun fault, northern Tibet, China. Bulletin of the Seismological Society of America, 95(5), 1970-1987.

Klinger, Y., Okubo, K., Vallage, A., Champenois, J., Delorme, A., Rougier, E., ... & Bhat, H. S. (2018). Earthquake damage patterns resolve complex rupture

processes. Geophysical Research Letters, 45(19), 10-279.

Lal, D. (1991). Cosmic ray labeling of erosion surfaces: in situ nuclide production rates and erosion models. *Earth and Planetary Science Letters*, *104*(2), 424–439. https://doi.org/10.1016/0012-821X(91)90220-C

Lavé, J., & Avouac, J. P. (2000). Active folding of fluvial terraces across the Siwaliks Hills, Himalayas of central Nepal. *Journal of Geophysical Research: Solid Earth*, *105*(B3), 5735–5770. https://doi.org/10.1029/1999JB900292.

Le Dortz, K., Meyer, B., Sébrier, M., Braucher, R., Bourlès, D., Benedetti, L. (2012). Interpreting scattered in-situ produced cosmogenic nuclide depth-profile data. Quaternary Geochronology, 11, 98-115.

Li Kang, Xu Xi-wei, Luo Hao, Paul Tapponnier, Yann Klinger, Gao Ming-xing. (2016). Paleoseismic events in banguoba trench along aksay segment of the Altyn Tagh fault zone. Seismology and Geology, 38(3): 670-679 (in Chinese).

Lin, X., Zheng, D., Sun, J., Windley, B. F., Tian, Z., Gong, Z., & Jia, Y. (2015). Detrital apatite fission track evidence for provenance change in the Subei Basin and implications for the tectonic uplift of the Danghe Nan Shan (NW China) since the mid-Miocene. *Journal of Asian Earth Sciences*, *111*, 302–311. https://doi.org/10.1016/j.jseaes.2015.07.007

Liu, J., Ren, Z., Zheng, W., Min, W., Li, Z., & Zheng, G. (2020). Late Quaternary slip rate of the Aksay segment and its rapidly decreasing gradient along the Altyn Tagh fault. *Geosphere*, *16*(6), 1538–1557. https://doi.org/10.1130/GES02250.1

Liu-Zeng, J., Klinger, Y., Sieh, K., Rubin, C., & Seitz, G. (2006). Serial ruptures of the San Andreas fault, Carrizo Plain, California, revealed by three‐dimensional excavations. Journal of Geophysical Research: Solid Earth, 111(B2). https://doi.org/10.1029/2004JB003601

1080 Luo, H., He, W., Yuan, D., & Shao, Y. (2015). Slip Rate of Yema River–Daxue
1081 Mountain Fault since the Late Pleistocene and Its Implications on the
1082 Deformation of the Northeastern Margin of the Tibetan Plateau. Acta Geologica
1083 Sinica - English Edition, 89(2), 561–574. https://doi.org/10.1111/1755-
1084 6724.12447
1085 Luo, H., Xu, X., Gao, Z., Liu, X., Yu, H., & Wu, X. (2019). Spatial and temporal
1086 distribution of earthquake ruptures in the eastern segment of the Altyn Tagh fault,
1087 China. Journal of Asian Earth Sciences, 173, 263-274.
1088 Matrau, R., Klinger, Y., Woerd, J. V. der, Liu-Zeng, J., Li, Z., Xu, X., & Zheng, R.
1089 (2019). Late Pleistocene-Holocene Slip Rate Along the Hasi Shan Restraining
1090 Bend of the Haiyuan Fault: Implication for Faulting Dynamics of a Complex
1091 Fault System. *Tectonics*, *38*(12), 4127–4154.
1092 https://doi.org/10.1029/2019TC005488
1093 Mériaux, A.-S., Tapponnier, P., Ryerson, F. J., Xiwei, X., King, G., Van der Woerd,
1094 J., et al. (2005). The Aksay segment of the northern Altyn Tagh fault: Tectonic
1095 geomorphology, landscape evolution, and Holocene slip rate. *Journal of*
1096 *Geophysical Research: Solid Earth*, *110*(B4).
1097 https://doi.org/10.1029/2004JB003210
1098 Merritts, D. J., Vincent, K. R., & Wohl, E. E. (1994). Long river profiles, tectonism,
1099 and eustasy: A guide to interpreting fluvial terraces. Journal of Geophysical
1100 Research: Solid Earth, 99(B7), 14031-14050.
1101 Métivier, F., Gaudemer, Y., Tapponnier, P., & Meyer, B. (1998). Northeastward
1102 growth of the Tibet plateau deduced from balanced reconstruction of two
1103 depositional areas: The Qaidam and Hexi Corridor basins, China. *Tectonics*,
1104 *17*(6), 823–842. https://doi.org/10.1029/98TC02764

1105 Meyer, B., Tapponnier, P., Bourjot, L., Métivier, F., Gaudemer, Y., Peltzer, G., et al.
1106 (1998). Crustal thickening in Gansu-Qinghai, lithospheric mantle subduction, and
1107 oblique, strike-slip controlled growth of the Tibet plateau. *Geophysical Journal*
1108 *International*, *135*(1), 1–47. https://doi.org/10.1046/j.1365-246X.1998.00567.x
1109 Meyer, Bertrand. (1991). *Mécanismes des grands tremblements de terre et du*
1110 *raccourcissement crustal oblique au bord nord-est du Tibet* (PhD Thesis). Paris 6.
1111 Peltzer, G., & Tapponnier, P. (1988). Formation and evolution of strike-slip faults,
1112 rifts, and basins during the India-Asia Collision: An experimental approach.
1113 *Journal of Geophysical Research: Solid Earth*, *93*(B12), 15085–15117.
1114 https://doi.org/10.1029/JB093iB12p15085
1115 Peltzer, G., Tapponnier, P., Gaudemer, Y., Meyer, B., Guo, S., Yin, K., et al. (1988).
1116 Offsets of late Quaternary morphology, rate of slip, and recurrence of large
1117 earthquakes on the Chang Ma fault (Gansu, China). *Journal of Geophysical*
1118 *Research: Solid Earth*, *93*(B7), 7793–7812.
1119 Peltzer, G., Tapponnier, P., & Armijo, R. (1989). Magnitude of late Quaternary left-
1120 lateral displacements along the north edge of Tibet. Science, 246(4935), 1285-
1121 1289.
1122 Peltzer, G., Crampé, F., & King, G. (1999). Evidence of nonlinear elasticity of the
1123 crust from the Mw7. 6 Manyi (Tibet) earthquake. Science, 286(5438), 272-276.
1124 Perrineau, A., Van Der Woerd, J., Gaudemer, Y., Liu-Zeng, J., Pik, R., Tapponnier, P.,
1125 et al. (2011). Incision rate of the Yellow River in Northeastern Tibet constrained
1126 by 10Be and 26Al cosmogenic isotope dating of fluvial terraces: implications for
1127 catchment evolution and plateau building. *Geological Society, London, Special*
1128 *Publications*, *353*(1), 189–219.
1129 Poisson, B., & Avouac, J.-P. (2004). Holocene hydrological changes inferred from

1130 alluvial stream entrenchment in north Tian Shan (northwestern China). *The*
1131 *Journal of Geology*, *112*(2), 231–249.
1132 Reimer, P. J., Bard, E., Bayliss, A., Beck, J. W., Blackwell, P. G., Ramsey, C. B., et al.
1133 (2013). IntCal13 and Marine13 radiocarbon age calibration curves 0–50,000
1134 years cal BP. *Radiocarbon*, *55*(4), 1869–1887.
1135 Reitman, N. G., Bennett, S. E. K., Gold, R. D., Briggs, R. W., & DuRoss, C. B.
1136 (2015). High-Resolution Trench Photomosaics from Image-Based Modeling:
1137 Workflow and Error AnalysisHigh-Resolution Trench Photomosaics from Image-
1138 Based Modeling: Workflow and Error Analysis. *Bulletin of the Seismological*
1139 *Society of America*, *105*(5), 2354–2366. https://doi.org/10.1785/0120150041
1140 Rizza, M., Bollinger, L., Sapkota, S. N., Tapponnier, P., Klinger, Y., Karakaş, Ç., et
1141 al. (2019). Post Earthquake Aggradation Processes to Hide Surface Ruptures in
1142 Thrust Systems: The M8.3, 1934, Bihar-Nepal Earthquake Ruptures at Charnath
1143 Khola (Eastern Nepal). *Journal of Geophysical Research: Solid Earth*, *124*(8),
1144 9182–9207. https://doi.org/10.1029/2018JB016376
1145 Rockwell, T. K., E. A. Keller, and G. R. Dembroff (1988). Quaternary rate of folding of the
1146 Ventura Avenue anticline, Western Transverse Ranges, southern California. Geological
1147 Society of America Bulletin, 100(6), 850–858. http://doi.org/10.1130/0016-
1148 7606(1988)100<0850:QROFOT>2.3.CO;2
1149 Ryerson, F. J., Tapponnier, P., Finkel, R. C., Mériaux, A.-S., Woerd, J. V. der,
1150 Lasserre, C., et al. (2006). Applications of morphochronology to the active
1151 tectonics of Tibet. https://doi.org/10.1130/2006.2415(05)
1152 Seong, Y. B., Kang, H. C., Ree, J.-H., Yi, C., & Yoon, H. (2011). Constant slip rate
1153 during the late Quaternary along the Sulu He segment of the Altyn Tagh Fault
1154 near Changma, Gansu, China. *Island Arc*, *20*(1), 94–106.

https://doi.org/10.1111/j.1440-1738.2010.00743.x

Shao, Y., Yuan, D., Oskin, M. E., Wang, P., Liu-Zeng, J., Li, C., & Wu, Z. (2017). Historical (Yuan Dynasty) Earthquake on the North Danghe Nanshan Thrust, Western Qilian Shan, ChinaHistorical (Yuan Dynasty) Earthquake on the North Danghe Nanshan Thrust, Western Qilian Shan, China. *Bulletin of the Seismological Society of America*, *107*(3), 1175–1184. https://doi.org/10.1785/0120160289

Shao, Y., Liu-Zeng, J., Van der Woerd, J., Klinger, Y., Oskin, M. E., Zhang, J., et al. (2021). Late Pleistocene slip rate of the central Haiyuan fault constrained from optically stimulated luminescence, 14C, and cosmogenic isotope dating and high-resolution topography. *GSA Bulletin*, *133*(7–8), 1347–1369. https://doi.org/10.1130/B35571.1

Shi, X., Tapponnier, P., Wang, T., Wei, S., Wang, Y., Wang, X., & Jiao, L. (2019). Triple junction kinematics accounts for the 2016 Mw 7.8 Kaikoura earthquake rupture complexity. Proceedings of the National Academy of Sciences, 116(52), 26367-26375.

Sieh, K. E., & Jahns, R. H. (1984). Holocene activity of the San Andreas fault at Wallace creek, California. Geological Society of America Bulletin, 95(8), 883-896.

Simoes, M., Avouac, J. P., & Chen, Y. G. (2007). Slip rates on the Chelungpu and Chushiang thrust faults inferred from a deformed strath terrace along the Dungpuna river, west central Taiwan. Journal of Geophysical Research: Solid Earth, 112(B3). https://doi.org/10.1029/2005JB004200

Stein, R. S., Barka, A. A., & Dieterich, J. H. (1997). Progressive failure on the North Anatolian fault since 1939 by earthquake stress triggering. Geophysical Journal

1180 International, 128(3), 594-604.
1181 Stockmeyer, J. M., Shaw, J. H., & Guan, S. (2014). Seismic hazards of multisegment
1182 thrust fault ruptures: Insights from the 1906 Mw 7.4–8.2 Manas, China,
1183 earthquake. *Seismological Research Letters*, *85*(4), 801–808.
1184 https://doi.org/10.1785/0220140026
1185 Stone, J. O. (2000). Air pressure and cosmogenic isotope production. Journal of
1186 Geophysical Research: Solid Earth, 105(B10), 23753-23759.
1187 Sun, J., Zhu, R., & An, Z. (2005). Tectonic uplift in the northern Tibetan Plateau since
1188 13.7 Ma ago inferred from molasse deposits along the Altyn Tagh Fault. *Earth*
1189 *and Planetary Science Letters*, *235*(3), 641–653.
1190 https://doi.org/10.1016/j.epsl.2005.04.034
1191 Suppe, J., & Medwedeff, D. A. (1990). Geometry and kinematics of fault-propagation
1192 folding. Eclogae Geologicae Helvetiae, 83(3), 409-454.
1193 Tapponnier, P., Meyer, B., Avouac, J. P., Peltzer, G., Gaudemer, Y., Guo Shunmin, et
1194 al. (1990). Active thrusting and folding in the Qilian Shan, and decoupling
1195 between upper crust and mantle in northeastern Tibet. *Earth and Planetary*
1196 *Science Letters*, *97*(3), 382–403. https://doi.org/10.1016/0012-821X(90)90053-Z
1197 Tapponnier, P., & Molnar, P. (1977). Active faulting and tectonics in China. Journal
1198 of Geophysical Research, 82(20), 2905-2930.
1199 Tapponnier, P., Zhiqin, X., Roger, F., Meyer, B., Arnaud, N., Wittlinger, G., &
1200 Jingsui, Y. (2001). Oblique Stepwise Rise and Growth of the Tibet Plateau.
1201 *Science*, *294*(5547), 1671–1677. https://doi.org/10.1126/science.105978
1202 Thompson, S. C., Weldon, R. J., Rubin, C. M., Abdrakhmatov, K., Molnar, P., &
1203 Berger, G. W. (2002). Late Quaternary slip rates across the central Tien Shan,
1204 Kyrgyzstan, central Asia. Journal of Geophysical Research: Solid Earth, 107(B9),

ETG-7.

van der Woerd, J. (1998). Kinematic Coupling between Active Strike-Slip and Thrust Faults in Northeast Tibet. Growth of the Tibet Plateau:[Dissertation]. Universite Paris, Paris.

van der Woerd, J., Ryerson, F. J., Tapponnier, P., Gaudemer, Y., Finkel, R., Meriaux, A. S., et al. (1998). Holocene left-slip rate determined by cosmogenic surface dating on the Xidatan segment of the Kunlun fault (Qinghai, China). *Geology*, *26*(8), 695–698. https://doi.org/10.1130/0091-7613(1998)026<0695:HLSRDB>2.3.CO;2

van der Woerd, J., Xu, X., Li, H., Tapponnier, P., Meyer, B., Ryerson, F. J., et al. (2001). Rapid active thrusting along the northwestern range front of the Tanghe Nan Shan (western Gansu, China). *Journal of Geophysical Research: Solid Earth*, *106*(B12), 30475–30504. https://doi.org/10.1029/2001JB000583

van der Woerd, J., Tapponnier, P., J. Ryerson, F., Meriaux, A.-S., Meyer, B., Gaudemer, Y., et al. (2002). Uniform postglacial slip-rate along the central 600 km of the Kunlun Fault (Tibet), from 26Al, 10Be, and 14C dating of riser offsets, and climatic origin of the regional morphology. *Geophysical Journal International*, *148*(3), 356–388. https://doi.org/10.1046/j.1365-246x.2002.01556.x

Wang, Y., Oskin, M. E., Zhang, H., Li, Y., Hu, X., & Lei, J. (2020). Deducing Crustal-Scale Reverse-Fault Geometry and Slip Distribution From Folded River Terraces, Qilian Shan, China. *Tectonics*, *39*(1), e2019TC005901. https://doi.org/10.1029/2019TC005901

Wang, M., & Shen, Z. K. (2020). Present‐day crustal deformation of continental China derived from GPS and its tectonic implications. Journal of Geophysical

1230 Research: Solid Earth, 125(2), e2019JB018774.
1231 https://doi.org/10.1029/2019JB018774
1232 Weldon, R. J. I. I., Scharer, K., Fumal, T., & Biasi, G. (2004). Wrightwood and the
1233 earthquake cycle: What a long recurrence record tells us about how faults work.
1234 GSA today, 14(9), 4-10.
1235 Wells, D. L., & Coppersmith, K. J. (1994). New empirical relationships among
1236 magnitude, rupture length, rupture width, rupture area, and surface displacement.
1237 *Bulletin of the Seismological Society of America*, *84*(4), 974–1002.
1238 Wittlinger, G., Vergne, J., Tapponnier, P., Farra, V., Poupinet, G., Jiang, M., et al.
1239 (2004). Teleseismic imaging of subducting lithosphere and Moho offsets beneath
1240 western Tibet. Earth and Planetary Science Letters, 221(1-4), 117-130.
1241 Wu, M., He, W., Zhang, B., Wang, P. & Liu, X. (2017). Investigation of Late
1242 Quaternary Activity along Subei Fault. China Earthquake Engineering Journal, 2,
1243 285–293 (in Chinese)
1244 Xu, Q., Hetzel, R., Hampel, A., & Wolff, R. (2021). Slip Rate of the Danghe Nan
1245 Shan Thrust Fault from 10Be Exposure Dating of Folded River Terraces:
1246 Implications for the Strain Distribution in Northern Tibet. Tectonics, 40(4),
1247 e2020TC006584. https://doi.org/10.1029/2020TC006584
1248 Xiao, Q., Yu, G., Liu-Zeng, J., Oskin, M. E., & Shao, G. (2017). Structure and
1249 geometry of the Aksay restraining double bend along the Altyn Tagh Fault,
1250 northern Tibet, imaged using magnetotelluric method. *Geophysical Research*
1251 *Letters*, *44*(9), 4090–4097.
1252 Xu, X., Wang, F., Zheng, R., Chen, W., Ma, W., Yu, G., et al. (2005). Late
1253 Quaternary sinistral slip rate along the Altyn Tagh fault and its structural
1254 transformation model. *Science in China Series D: Earth Sciences*, *48*(3), 384.

https://doi.org/10.1360/02yd0436

Xu, X., Wen, X., Yu, G., Chen, G., Klinger, Y., Hubbard, J., & Shaw, J. (2009). Coseismic reverse- and oblique-slip surface faulting generated by the 2008 Mw 7.9 Wenchuan earthquake, China. *Geology*, *37*(6), 515–518. https://doi.org/10.1130/G25462A.1

Xu, X., Yeats, R. S., & Yu, G. (2010). Five Short Historical Earthquake Surface Ruptures near the Silk Road, Gansu Province, China. *Bulletin of the Seismological Society of America*, *100*(2), 541–561. https://doi.org/10.1785/0120080282

Yang, H., Yang, X., Zhang, H., Huang, X., Huang, W., & Zhang, N. (2018). Active fold deformation and crustal shortening rates of the Qilian Shan Foreland Thrust Belt, NE Tibet, since the Late Pleistocene. Tectonophysics, 742, 84-100.

Yang, Y., Liu, C.-Q., Van der Woerd, J., Xu, S., Cui, L.-F., Zhao, Z.-Q., et al. (2019). New constraints on the late Quaternary landscape evolution of the eastern Tibetan Plateau from 10Be and 26Al in-situ cosmogenic nuclides. *Quaternary Science Reviews*, *220*, 244–262. https://doi.org/10.1016/j.quascirev.2019.07.020

Yin, A., Rumelhart, P. E., Butler, R., Cowgill, E., Harrison, T. M., Foster, D. A., et al. (2002). Tectonic history of the Altyn Tagh fault system in northern Tibet inferred from Cenozoic sedimentation. *GSA Bulletin*, *114*(10), 1257–1295. https://doi.org/10.1130/0016-7606(2002)114<1257:THOTAT>2.0.CO;2

Yin, An, Dang, Y.-Q., Wang, L.-C., Jiang, W.-M., Zhou, S.-P., Chen, X.-H., et al. (2008). Cenozoic tectonic evolution of Qaidam basin and its surrounding regions (Part 1): The southern Qilian Shan-Nan Shan thrust belt and northern Qaidam basin. *GSA Bulletin*, *120*(7–8), 813–846. https://doi.org/10.1130/B26180.1

Yu, J., Zheng, D., Pang, J., Wang, Y., Fox, M., Vermeesch, P., et al. (2019). Miocene

1280 Range Growth Along the Altyn Tagh Fault: Insights From Apatite Fission Track
1281 and (U-Th)/He Thermochronometry in the Western Danghenan Shan, China.
1282 *Journal of Geophysical Research: Solid Earth*, *0*(0).
1283 https://doi.org/10.1029/2019JB017570
1284 Zhang, P.-Z., Molnar, P., & Xu, X. (2007). Late Quaternary and present-day rates of
1285 slip along the Altyn Tagh Fault, northern margin of the Tibetan Plateau.
1286 *Tectonics*, *26*(5). https://doi.org/10.1029/2006TC002014
1287 Zheng, D., Clark, M. K., Zhang, P., Zheng, W., & Farley, K. A. (2010). Erosion, fault
1288 initiation and topographic growth of the North Qilian Shan (northern Tibetan
1289 Plateau). *Geosphere*, *6*(6), 937–941. https://doi.org/10.1130/GES00523.1
1290 Zheng, W., Zhang, P., He, W., Yuan, D., Shao, Y., Zheng, D., et al. (2013).
1291 Transformation of displacement between strike-slip and crustal shortening in the
1292 northern margin of the Tibetan Plateau: Evidence from decadal GPS
1293 measurements and late Quaternary slip rates on faults. *Tectonophysics*, *584*, 267–
1294 280. https://doi.org/10.1016/j.tecto.2012.01.006
1295 Zhou, J., Xu, F., Wang, T., Cao, A., & Yin, C. (2006). Cenozoic deformation history
1296 of the Qaidam Basin, NW China: Results from cross-section restoration and
1297 implications for Qinghai–Tibet Plateau tectonics. *Earth and Planetary Science*
1298 *Letters*, *243*(1), 195–210. https://doi.org/10.1016/j.epsl.2005.11.033
1299 Zhuang, G., Hourigan, J. K., Ritts, B. D., & Kent-Corson, M. L. (2011). Cenozoic
1300 multiple-phase tectonic evolution of the northern Tibetan Plateau: Constraints
1301 from sedimentary records from Qaidam basin, Hexi Corridor, and Subei basin,
1302 northwest China. *American Journal of Science*, *311*(2), 116–152.
1303 https://doi.org/10.2475/02.2011.02
1304 Zuza, A. V., Wu, C., Reith, R. C., Yin, A., Li, J., Zhang, J., et al. (2018). Tectonic

1305 evolution of the Qilian Shan: An early Paleozoic orogen reactivated in the
1306 Cenozoic. GSA Bulletin, 130(5–6), 881–925. https://doi.org/10.1130/B31721.1
1307 He W.G., Zhang B., Wu M., Wang P.T., Zou X.B., Gao X.D. (2018).
1308 Paleoseismology on the Yemahe segment of the Yemahe-Daxueshan fault
1309 revealed by trench study. Seismology and Geology, 40(1): 261-275.

1310
1311
1312
1313
1314
1315

1316 Table 1. Terrace heights and vertical offset estimates

Terrace	Profile	Height above river bed upstream (m)	Maximum height above river bed (m)	Vertical offset relative to downstream fan (m)
Site 1				Relative to Tf2
T1	b-b’		7.5±0.5	-
T2	p3/c-c’	18±1	23±1	15±1
T3	p4/d-d’	27±2	40±2	31±2
T4	P2/e-e’	50±3	60±3	50±3
Site 2				
T1	pf2			1.5±0.2
T1’	pf3			1.6±0.2
T2’	pf4			3.5±0.5
Tf2	pf1			2.6±0.3
	pf5			3.6±0.5

1317
1318

1319 Table 2. Optically stimulated luminescence (OSL) analytical data

Sample No	Lab. no[a]	Depth(m)	Water content[b] (%)	U(ppm)	Th(ppm)	K(%)	Cosmic dose rate(Gy/ka)	grain size (μm)	Dose rate[c] (Gy/ka)	Equivalent dose[d] (Gy)	Age[e] (ka)
T1											
SB-OSL-1504	15-55	0.3	2.09	2.48±0.1	10.6±0.3	1.73±0.06	0.31±0.02	90-125	3.31±0.13	17.7±0.4	5.4±0.2
T2											
SB-OSL-1501	15-52	1.35	3.51	3.08±0.11	10.4±0.29	1.71±0.05	0.26±0.02	90-125	3.32±0.12	19.6±0.5	5.9±0.3
SB-OSL-1502	15-53	0.9	4.67	2.68±0.1	11±0.31	1.82±0.06	0.28±0.02	90-125	3.35±0.12	18.7±0.4	5.6±0.2
SB-OSL-1503	15-54	0.5	0.64	2.56±0.1	9.85±0.29	1.62±0.05	0.3±0.02	90-125	3.21±0.12	15.3±0.3	4.8±0.2
T3											
SB-OSL-1505	15-56	0.42	1.25	2.33±0.09	10.4±0.29	1.7±0.05	0.3±0.02	90-125	3.26±0.12	17±0.4	5.2±0.2
SB-OSL-1507	15-58	1.3	6.34	2.26±0.09	8.31±0.25	1.7±0.05	0.26±0.02	90-125	2.89±0.11	21.8±0.5	7.6±0.3
T4											
SB-OSL-1508	15-59	0.45	10.02	2.56±0.1	10.9±0.31	1.79±0.06	0.3±0.02	90-125	3.14±0.12	25.8±0.5	8.2±0.4

1320 a: All samples were processed at Zhejiang Zhongke Institute of Luminescence Testing Technology;
1321 b: Measured water content;
1322 c: Concentrations of U, Th and K were measured by neutron activation analysis at China institute of
1323 atomic energy;
1324 d: All De values conform to normal distribution;
1325 e: All De values were calculated with central age model (Galbraith et al., 2012).

1326 Table 3. ^{10}Be analytical data for depth profiles at site 1 and surface boulders at site 2

Samples	Mass quartz (g)	Be Carrier (mg)	Latitude (N)	Longitude (E)	Altitude (m)	Depth (cm)	Thickness (cm)	Sample type	10Be/9Be	10Be/9Be error (%)	10Be ± error (atom/g)	Exposure age ± uncertainty (yr)
Site 1												
T1 depth profile												
T101	19.082	0.259	39.4644	94.8154	2550	4	5	gravel	1.99743E-13	2.84493542	139215±3966	See model
T102	18.3446	0.2622	39.4644	94.8154	2550	23.5	5	gravel	2.34437E-13	3.16617704	179736±5698	/
T103	24.6633	0.2619	39.4644	94.8154	2550	38.5	5	gravel	2.79777E-13	2.81553863	165707±4672	/
T104	23.5114	0.2604	39.4644	94.8154	2550	66.5	5	gravel	2.11103E-13	3.21317004	122006±3925	/
T105	16.2753	0.2628	39.4644	94.8154	2550	112	5	gravel	1.58258E-13	4.50561624	120855±5453	/
T106	19.9296	0.2597	39.4644	94.8154	2550	162	5	gravel	1.06914E-13	4.78682755	52823±2532	/
T107	24.7446	0.2595	39.4644	94.8154	2550	202	5	gravel	1.63803E-13	3.32730129	82378±2745	/
T2 depth profile												
T201	26.985	0.2572	39.46584	94.81676	2543	146.5	5	gravel	2.88702E-13	2.80433717	156347±4390	See model
T202	18.6568	0.2644	39.46584	94.81676	2543	160	5	gravel	2.16697E-13	2.79024612	164281±4590	/
T203	29.7611	0.2625	39.46584	94.81676	2543	192.5	5	gravel	1.96218E-13	10.6339378	90175±9602	/
T204	24.0209	0.2505	39.46584	94.81676	2543	221.5	5	gravel	2.47250E-13	3.86466734	150008±5805	/
T207	29.7902	0.2592	39.46584	94.81676	2543	342.5	5	gravel	1.57479E-13	4.58115034	72964±3347	/
T3 depth profile												
T301	30.002	0.2603	39.46587	94.81474	2571	132.5	5	gravel	1.79830E-12	5.06926063	1019912±51771	See model
T302	30.1499	0.2621	39.46587	94.81474	2571	162.5	5	gravel	1.77618E-12	1.48973645	1009077±15053	/
T305	30.1379	0.261	39.46587	94.81474	2571	252.5	5	gravel	5.58156E-13	7.55396228	300382±22721	/
T4 depth profile												
T402	30.0074	0.265	39.46608	94.81159	2616	68.5	5	gravel	3.13757E-12	1.77849721	1831441±32615	See model
T403	31.7724	0.2616	39.46608	94.81159	2616	98.5	5	gravel	3.08259E-12	1.3182097	1677233±22139	/
T404	29.6724	0.2619	39.46608	94.81159	2616	131.5	5	gravel	1.98844E-12	1.77949615	1152668±20539	/
T405	31.3068	0.2554	39.46608	94.81159	2616	161	5	gravel	1.25525E-12	4.89009314	665693±32596	/
T406	30.4697	0.2693	39.46608	94.81159	2616	191	5	gravel	1.29302E-12	3.78535521	743514±28182	/
T407	32.4745	0.2627	39.46608	94.81159	2616	221	5	gravel	5.47390E-13	2.53345878	277465±7039	/
Site 2 surface												
LP01	30.7098	0.308	39.47123	94.90786	2265	0	2.5	boulder	1.02453E-12	6.32872596	670639±42500	28133±3040
LP02	30.2138	0.3154	39.47112	94.90761	2265	0	2.5	boulder	5.48760E-13	5.84434137	366152±21428	15826±1661

LP03	27.7759	0.3149	39.47099	94.90705	2266	0	2.5	boulder	5.32490E-13	4.19369166	385332±16181	16603±1605
LP04	19.6304	0.3159	39.4708	94.90692	2267	0	2.5	boulder	3.52189E-13	3.21520471	353072±11367	15268±1416
LP05	23.0298	0.3157	39.47078	94.90681	2269	0	2.5	boulder	9.16409E-13	4.03025204	817601±32995	33799±3257
LP06	24.787	0.3178	39.47128	94.90797	2265	0	2.5	boulder	4.85817E-13	6.75410724	395787±26767	17042±1880

Note: AMS measurements were performed at ASTER in Centre de Recherche et d'Enseignement de Géosciences de l'Environnement (CEREGE), Aix-en-Provence, France. Surface ages at site 2 are calculated with the CRONUS 2.3 calculator (http://hess.ess.washington.edu/), with time-dependent Lal (1991) / Stone (2000) scaling scheme for spallation, sample density 2.7 g/cm^3, and no erosion. Reference production rate of ^{10}Be is 4.00±0.29 atoms / gram of quartz /year. (Borchers et al., 2016).

1333 Table 4. Radiocarbon analytical data

Sample No.	Percent Modern Carbon (pMC)	Fraction Modern	D14C	Conventional age	2 sigma calibration [c]
14C-1517 [a]	40.2 +/-0.2 pMC	0.4015±0.0015	-598.5 +/-1.5	7330 +/-30 BP	Cal BC 6240 to 6090 (Cal BP 8190 to 8040)
STH48c [b]		0.3901±0.0112		7500±240	8473±512 years B.P.
STH48d [b]		0.3605±0.0031	-639.5±3.1	8200±80	9163±158 years B.P.
STH48e [b]		0.3854±0.0044	-614.6±4.4	7660±100	8478±104 years B.P.
					Mean: 8705±557 years B.P.

1334 a: Sample AMS dated at Beta Analytic;
1335 b: Re-calibrated radiocarbon dates from van der Woerd et al. (2001) measured at Center for Accelerator Mass Spectrometry at Lawrence Livermore National Laboratory (Livermore, California, USA) in 1998.
1336 C Calibration with IntCal13 (Reimer et al., 2013), not including probability distribution of range < 0.1.
1337
1338
1339

1340
1341 Table 5. ^{10}Be depth profiles modeling parameters

Terrace name		Inheritance (atoms / g)	Stage 1	Stage 2	Stage 3
T1		150000	8.7 - 6 ka	6 - 5.6 ka	5.6 - 0 ka
T2		200000	9.5 - 6.1 ka	6.1 - 4.3 ka	4.3 - 0 ka
T3	Model 1	4000	67.6 - 7.6 ka	7.6 - 4.1 ka	4.1 - 0 ka
	Model 2	86000	41.6 - 7.6 ka	7.6 - 4.1 ka	4.1 - 0 ka
T4	Model 1	10000	128 - 8.2 ka	8.2 -0 ka	

1342
1343

Table 6. Shortening estimates from models 1 and 2 at site 1.

	Age (ka)	Height/T0 (m)	Vertical offset (m)	Min height /paleobaselevel (m)	Max height /paleobaselevel (m)	Area (m^2)	Depth (m)	Depth (m)	Ramp (°)	Slip on ramp (m)	Shortenning rate (mm/yr)	Vertical rat /T0 (mm/y
		Umax					Dα	D0	α	S		
Model 1						S1/A1						
T1	8.7±0.5	7.5±0.5	na			7138	1000	1000	0	7.1±0.5	0.84±0.1	0.82±0.09
T2	9.5±1	23±1	15±1			9190	1000	1000	0	9.2±0.5	0.97±0.12	2.42±0.11
T3	51.5±13.5	40±2	>31±2			33903	1000	1000	0	33.9±2	0.64±0.27	0.78±0.27
T4	128±20	60±3	>50±3			55316	1000	1000	0	55.3±3	0.51±0.16	0.55±0.16
Model 2				U	Umax	S2/A2						
T1	8.7±0.5	7.5±0.5	na	1.5±0.5	8.5±0.5	9933	1889	1889	23.5	3.8±0.5	0.44±0.14	0.82±0.09
T2	9.5±1	23±1	15±1	1.9±0.5	13±1	13817	1889	1889	23.5	4.8±0.5	0.50±0.15	2.42±0.11
T3	51.5±13.5	40±2	>31±2	13±1	56±3	59480	1889	1889	23.5	31.3±2	0.61±0.27	0.78±0.27
T4	128±20	60±3	>50±3	22±1	81±3	104684	1889	1889	23.5	55.2±3	0.43±0.16	0.55±0.16

Figure 1.

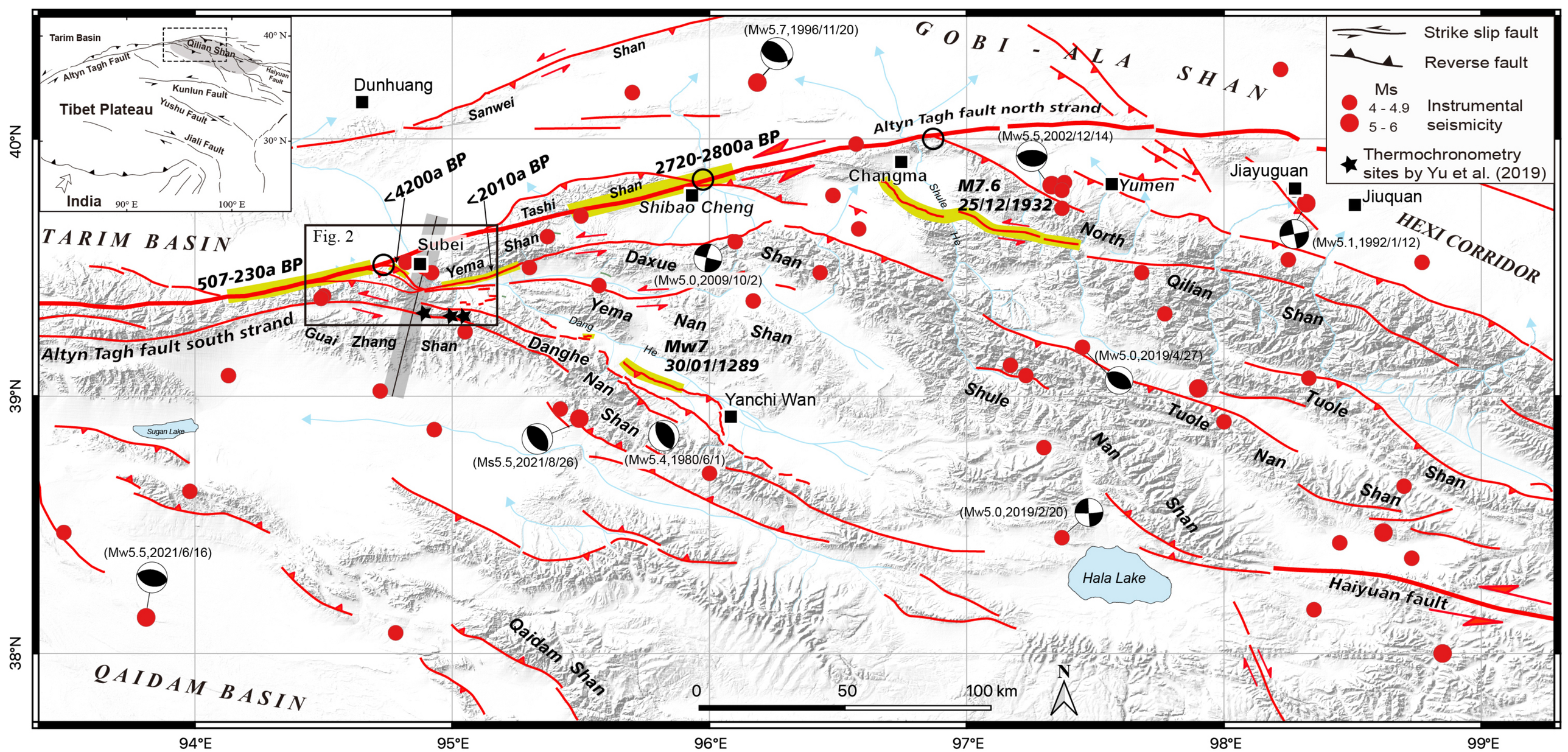
Tarim Basin
Qilian Shan
Altyn Tagh Fault
Kunlun Fault
Yushu Fault
Jiali Fault
Haiyuan Fault
Tibet Plateau
India
40° N
30° N
90° E
100° E
Strike slip fault
Reverse fault
Ms
4 - 4.9
5 - 6
Instrumental seismicity
Thermochronometry sites by Yu et al. (2019)
GOBI - ALA SHAN
TARIM BASIN
QAIDAM BASIN
HEXI CORRIDOR
Fig. 2
Dunhuang
Subei
Shibao Cheng
Changma
Yumen
Jiayuguan
Jiuquan
Yanchi Wan
Sugan Lake
Hala Lake
Altyn Tagh fault north strand
Altyn Tagh fault south strand
Sanwei Shan
Tashi Shan
Yema Shan
Guai Zhang Shan
Daxue Shan
Yema Dang Nan Shan
Danghe Nan Shan
Shule Nan Shan
Qilian Shan
Tuole Nan Shan
Haiyuan fault
Qaidam Shan
Shule He
North He
<4200a BP
<2010a BP
2720-2800a BP
507-230a BP
M7.6 25/12/1932
Mw7 30/01/1289
(Mw5.7,1996/11/20)
(Mw5.5,2002/12/14)
(Mw5.1,1992/1/12)
(Mw5.0,2009/10/2)
(Mw5.0,2019/4/27)
(Mw5.0,2019/2/20)
(Ms5.5,2021/8/26)
(Mw5.4,1980/6/1)
(Mw5.5,2021/6/16)
0
50
100 km
N
40°N
39°N
38°N
94°E
95°E
96°E
97°E
98°E
99°E

Figure 2.

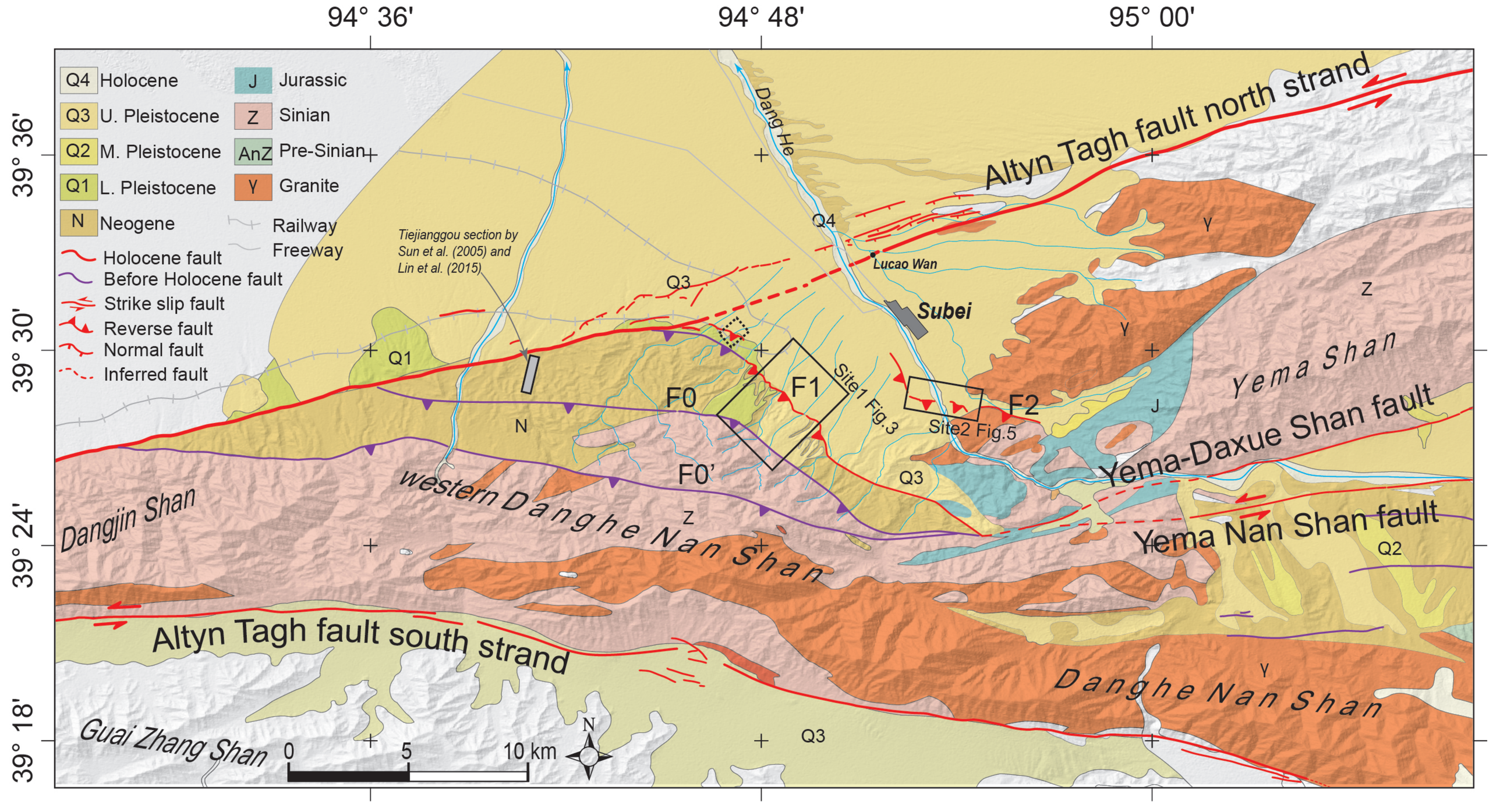
94° 36'
94° 48'
95° 00'
39° 36'
39° 30'
39° 24'
39° 18'
Q4 Holocene
Q3 U. Pleistocene
Q2 M. Pleistocene
Q1 L. Pleistocene
N Neogene
Holocene fault
Before Holocene fault
Strike slip fault
Reverse fault
Normal fault
Inferred fault
J Jurassic
Z Sinian
AnZ Pre-Sinian
γ Granite
Railway
Freeway
Tiejianggou section by Sun et al. (2005) and Lin et al. (2015)
Dang He
Altyn Tagh fault north strand
Lucao Wan
Subei
Site1 Fig.3
Site2 Fig.5
F0
F0'
F1
F2
Yema Shan
Yema-Daxue Shan fault
Yema Nan Shan fault
western Danghe Nan Shan
Danghe Nan Shan
Dangjin Shan
Altyn Tagh fault south strand
Guai Zhang Shan
0
5
10 km
N

Figure 3.

Model 1

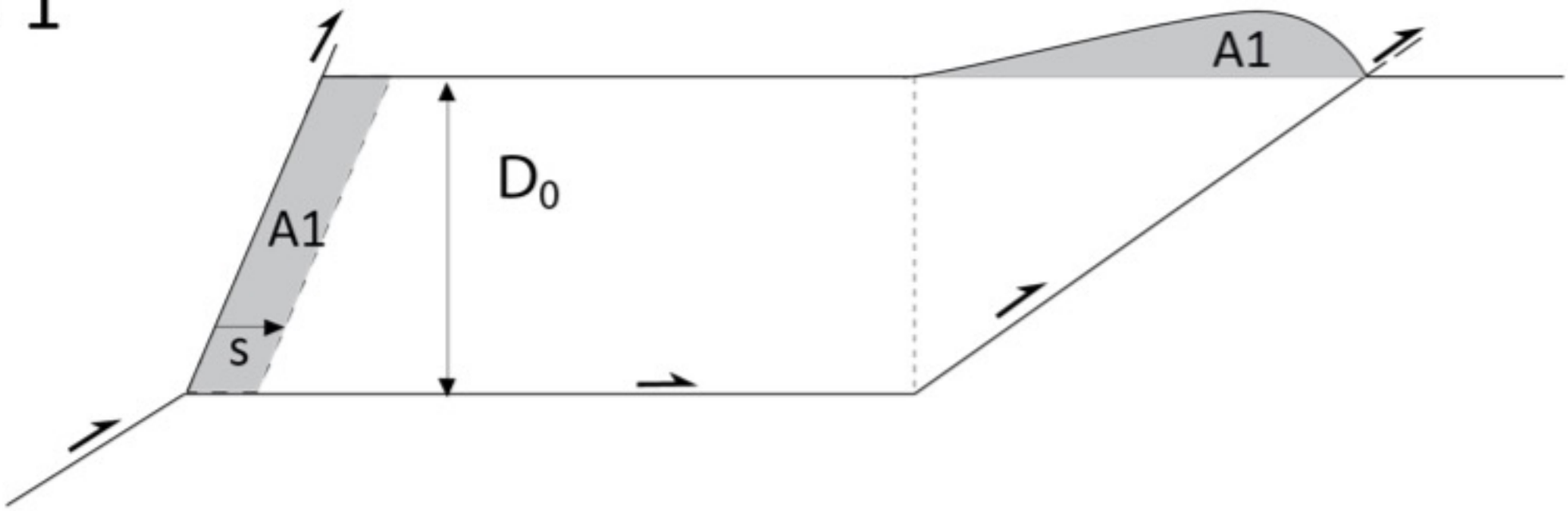

Model 2

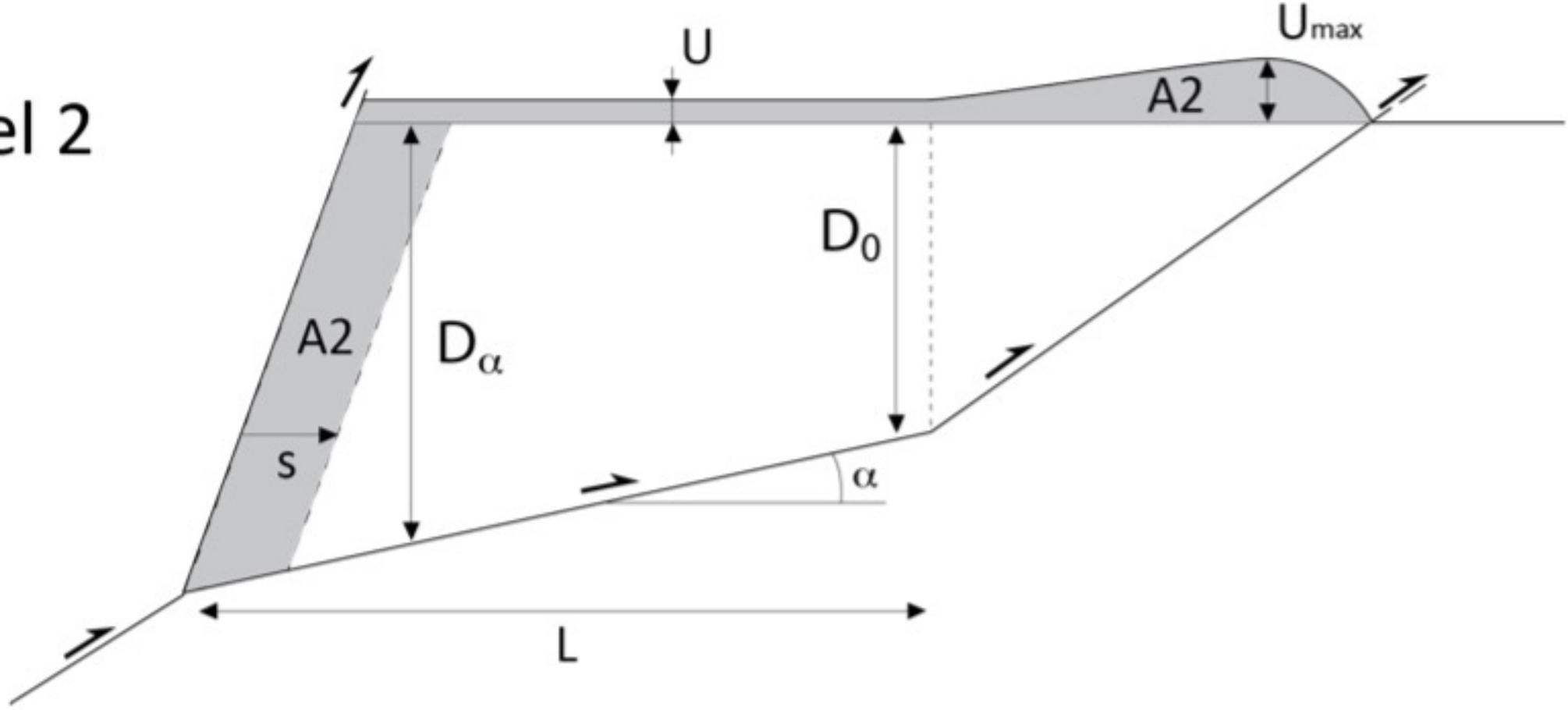

Figure 4.

a

b

Terraces:

T0 T1/Tf1 T2/Tf2 T3 T4

Thrusts

Topographic profiles by this study

Topographic profiles by Van der Woerd et al. (2001)

14C sampling site of Van der Woerd et al. (2001)

10Be depth profiles

94°49'

39°28'

39°27'

94°48'

p1

p2

p3

p4

e'

d'

c'

b'

a'

Tf1

Tf2

F1

F0

T2

T3

T4

r6

r5

a

b

c

d

e

Fig. 8A

Fig. 8D

Fig. 3C

N

500 m

c

T4

T3

T2

T1

T0

Subei

Figure 5.

a

e

r5

a

p2

p1

T4

6.9°

50±3 m

T0

p4

p3

6.8°

27±2 m

18±1 m

F0

b

T1

T2

T3

d

5.7°

60±3 m

c

b'

6.3°

d'c'

a'

5.4°

5.3°

Tf2

30±2 m

4.6°

e'

4.6°

4.6°

T0

F1

200 m
(x4)

1000 m

b

T4

6.2°

T3

60±3 m

T1

T2

40±2 m

6.4°

6.1°

T0

7.5±0.5 m

6.1°

6.3°

6.9°

6.1°

50±3 m

23±1 m

6.1°

31±2 m

15±1 m

8m

6.2°

Tf2

5m

F1

100 m
(x4)

500 m

Figure 6.

a

N

0 400 800 m

b

Fig.6B Fig.6A Fig.6C Fig.6D Fig.6E Fig.6F

Dang He

pf1 pf2 pf3 pf4 pf5 pf8 pf9

T1' F2 T2' T1 T2 T0 T3 r2

Tf2 Tf3

01 02 03 04 05 06

N

0 400 800 m

active faults
thrust
inferred
trench
active channel
profiles
Cosmogenic nuclide samples

c

Altitude 2252 m 2192

N

pf6 pf7 pf2 pf3 pf4 pf5

T1' T2' Tf2

0 250 500 m

d

10°

pf1 pf2 pf3 pf4 pf5

T1 T2 T1' T2' Tf2

2.3° 2.5° 1.8° 2.2°

1.5±0.2m 2.6±0.3m 1.6±0.2m 3.5±0.5m 3.6±0.5m

10 m

200 m

e

SE

pf6 T1' ~3m T2' Tf2

pf7 T1' ~3m T2' ~1m Tf2

10 m 8 6 4 2 0

0 200 400 m

EW

pf8 Tf3 Tf2 r2 T2 Danghe T1 T1' T2' Tf2

~37m ~33m ~24m ~12m ~29m ~34m ~5m

50 m 40 30 20 10 0

0 200 400 m

NE

pf9 T3 T2 Danghe T1 T2'

~60m ~36m ~13m ~43m

Figure 7.

a

Danghe Nanshan

T4

T4

~1.5 m

S

b

Danghe Nanshan

person

river bed

S

c

Danghe Nanshan

~2.6 m

person

S

d

~3.5 m

S

e

S

~0.5 m

f

N

Figure 8.

a

West wall

b

U1

U2

U3

f1

∠19°

f2

∠12°

2°

Colluvial wedge

55 cm

310 cm

∠7°

280 cm

120 cm

f3

∠19°

1m

1m

Area removed by farmer

14C1517

8190-8040 a BP

c

East wall

d

U1

U2

U3

f1

∠19°

f2

∠8°

2°

Colluvial wedge

50 cm

300 cm

90 cm

∠19°

f3

1m

1m

Area removed by farmer

Figure 9.

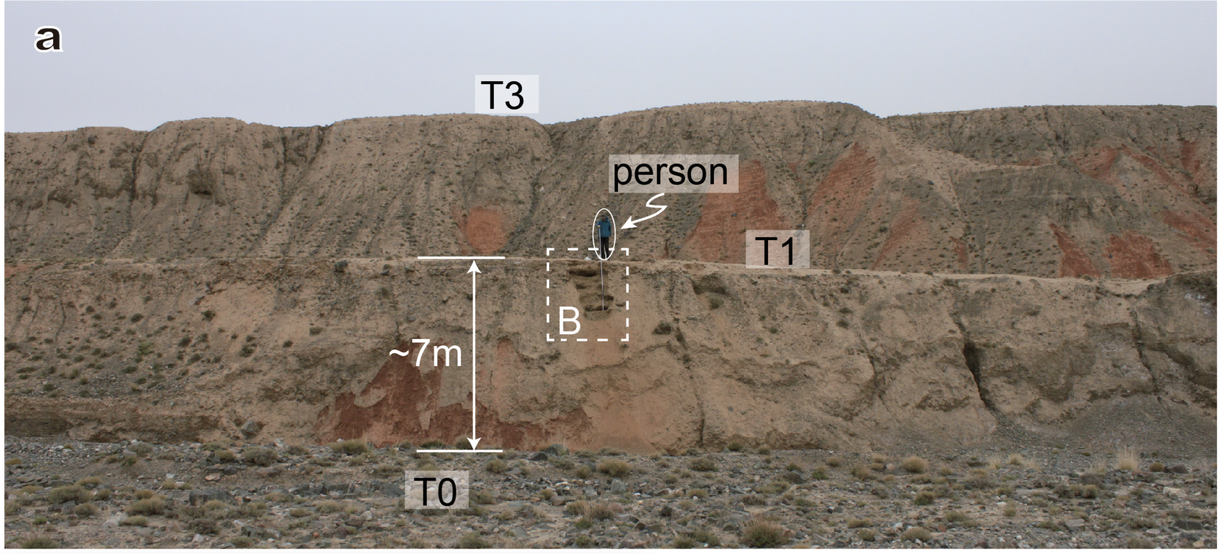
a
T3
person
T1
B
~7m
T0

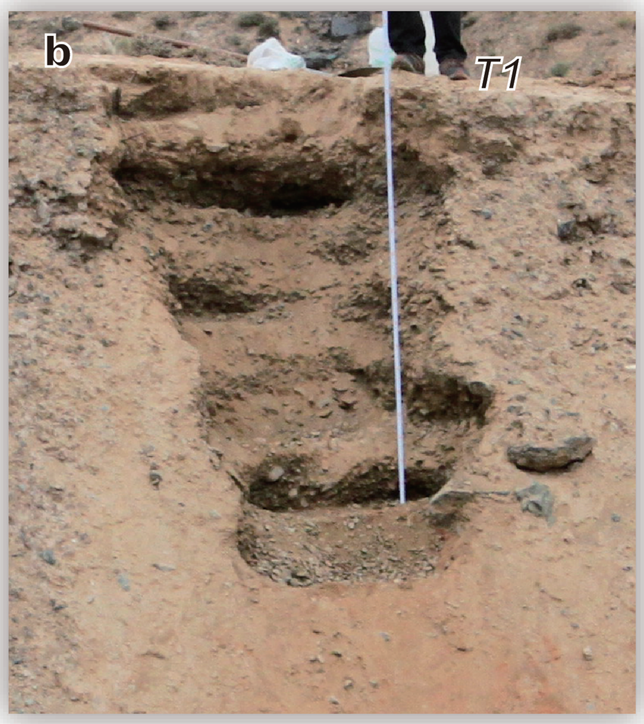
b
T1

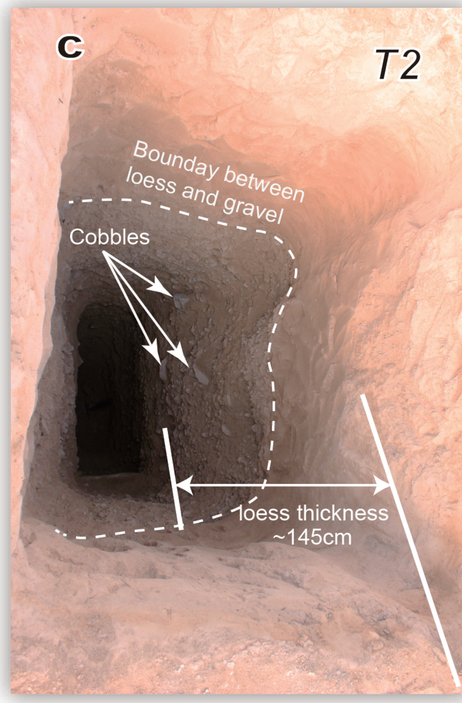
c
T2
Bounday between loess and gravel
Cobbles
loess thickness ~145cm

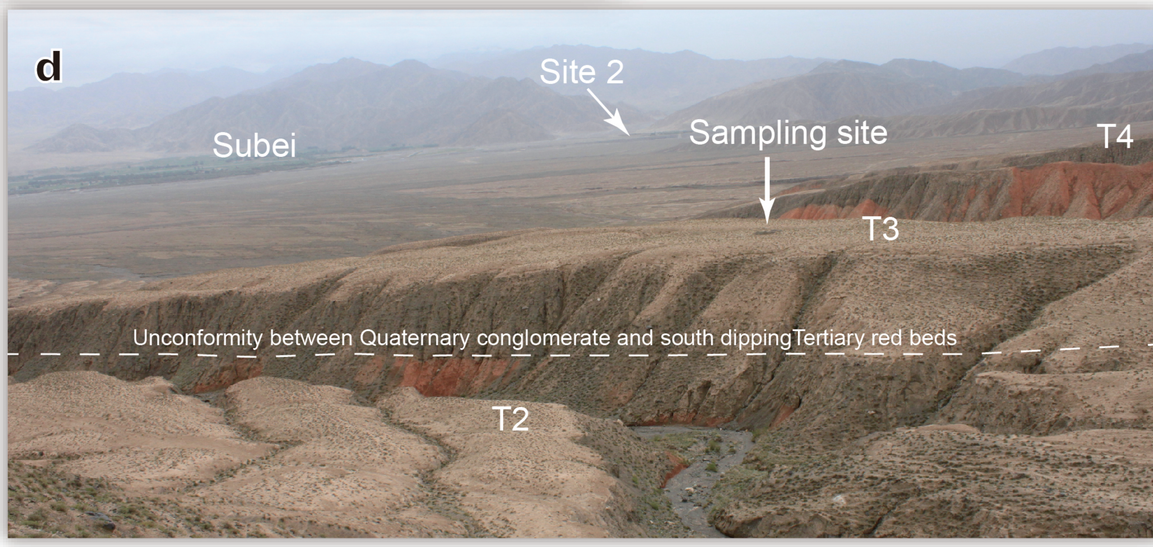
d
Site 2
Subei
Sampling site
T4
T3
Unconformity between Quaternary conglomerate and south dippingTertiary red beds
T2

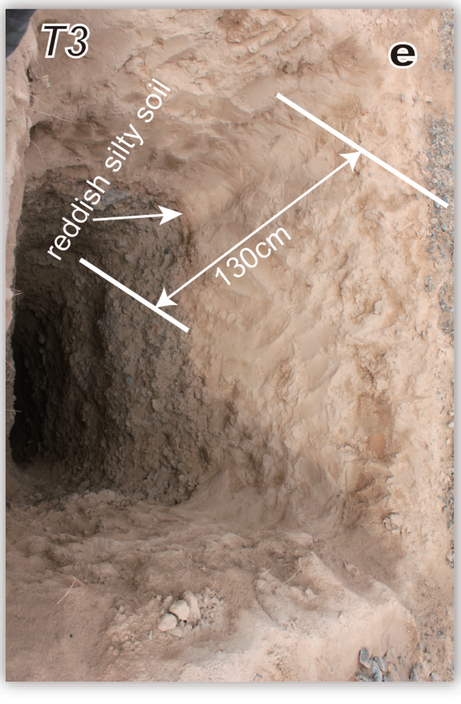
T3
e
reddish silty soil
130cm

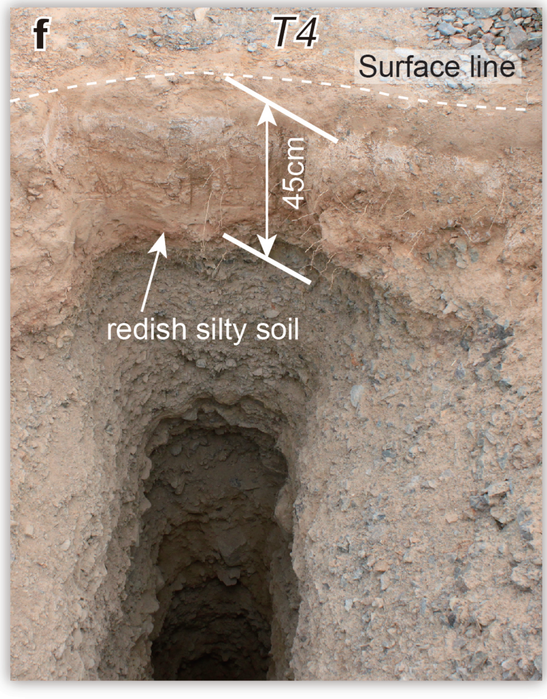
f
T4
Surface line
45cm
redish silty soil

Figure 10.

a

T1

SBOSL-1504 (5.4 +/- 0.2 ka)

Coarse sand and gravels
Thin (<10cm) loess layer

d=2.0
d=1.4

Massive coarse sand, gravel, rounded pebbles, mixed with few cobbles

d=2.0

South dipping (~50°) Tertiary red sandstones.

0
-0.5
-1
-1.5
-2
-2.5

SBTCN-T101
SBTCN-T102
SBTCN-T103
SBTCN-T104
SBTCN-T105
SBTCN-T106
SBTCN-T107

b

^{10}Be Concentration (at/g 10^4)

T1

0 5 10 15

Depth (m)

0 -0.5 -1 -1.5 -2 -2.5

SBTCN-T1-01
02
03
04
05
06
07

Upper section age: 5.6 ± 0.3 ka

Inheritance = 1.5×10^4 at/g

Lower section age: 8.7 ± 0.5 ka

R-squared = 0.99
Inheritance = 1.5×10^4 at/g
No erosion
Outliers

c

T2

Top yellowish-brown loess unit (145 cm thick)

SBOSL-1503 (4.8 +/- 0.2 ka)
SBOSL-1502 (5.6 +/- 0.2 ka)
SBOSL-1501 (5.9 +/- 0.3 ka)

d=1.4

Coarse sand with rounded pebbles and cobbles. Upward fining from 5 to 1 cm in upper part.

d=2.0

Lower part composed of pebbels. A few large cobbles.

0
-0.5
-1
-1.5
-2
-2.5
-3
-3.5

SBTCN-T201
SBTCN-T202
SBTCN-T203
SBTCN-T204
SBTCN-T207

d

^{10}Be Concentration (at/g 10^4)

T2

0 2 4 6 8 10 12 14 16 18

Depth (m)

0 -0.5 -1 -1.5 -2 -2.5 -3 -3.5

No inheritance

SBTCN-T2-01
02
03
04
07

Exposure age t2 = 9.5 ± 1 ka

R-squared = 0.99
Inheritance = 2×10^4 at/g
No erosion
Outliers

e

T3

Top loess about 130 cm thick

SBOSL-1505 (5.2 +/- 0.2 ka)

d=1.4

Reddish silty soil layer (few cm thick)

SBOSL-1507 (7.6 +/- 0.4 ka)

8705+/-557 years B.P. Recalibrated ages of same terrace from Van der Woerd et al. (2001)

d=2.2

Gravel with coare sand, pebbles and cobbles sizes change from 7, to 4, to 1-2, to 5-7cm from bottom to top.

0
-0.5
-1
-1.5
-2
-2.5
-3

SBTCN-T301
SBTCN-T302
SBTCN-T305

f

^{10}Be Concentration (at/g 10^5)

T3

0 2 4 6 8 10 12 14 16

Depth (m)

0 -0.5 -1 -1.5 -2 -2.5 -3

No inheritance

Model 1:

Exposure age t3 = 67.6 ± 10 ka

R-squared = 0.99
Inheritance = 0.4×10^4 at/g
No erosion

SBTCN-T3-01
02
05

Model 2

Model 1

Model 2:

Exposure age t3 = 41.6 ± 4 ka

R-squared = 0.99
Inheritance = 8.6×10^4 at/g
No erosion

g

T4

Top loess layer, (45 cm thick) above 2-3 cm redish silty soil

SBOSL-1508 (8.2 +/- 0.4 ka)

d=1.4

d=2.5

Angular gravel with coarse sand, pebbles and cobbles sizes from 2 to 7 cm, coarsening upward.

0
-0.5
-1
-1.5
-2
-2.5

SBTCN-T402
SBTCN-T403
SBTCN-T404
SBTCN-T405
SBTCN-T406
SBTCN-T407

h

^{10}Be Concentration (at/g 10^5)

T4

0 5 10 15 20 25 30 35

Depth (m)

0 -0.5 -1 -1.5 -2 -2.5

No inheritance

SBTCN-T4- 02
03
04
05
06
07

Exposure age t4 = 128 +/- 20 ka

R-squared = 0.97
Inheritance = 1×10^4 at/g
No erosion
Outliers

Figure 11.

a

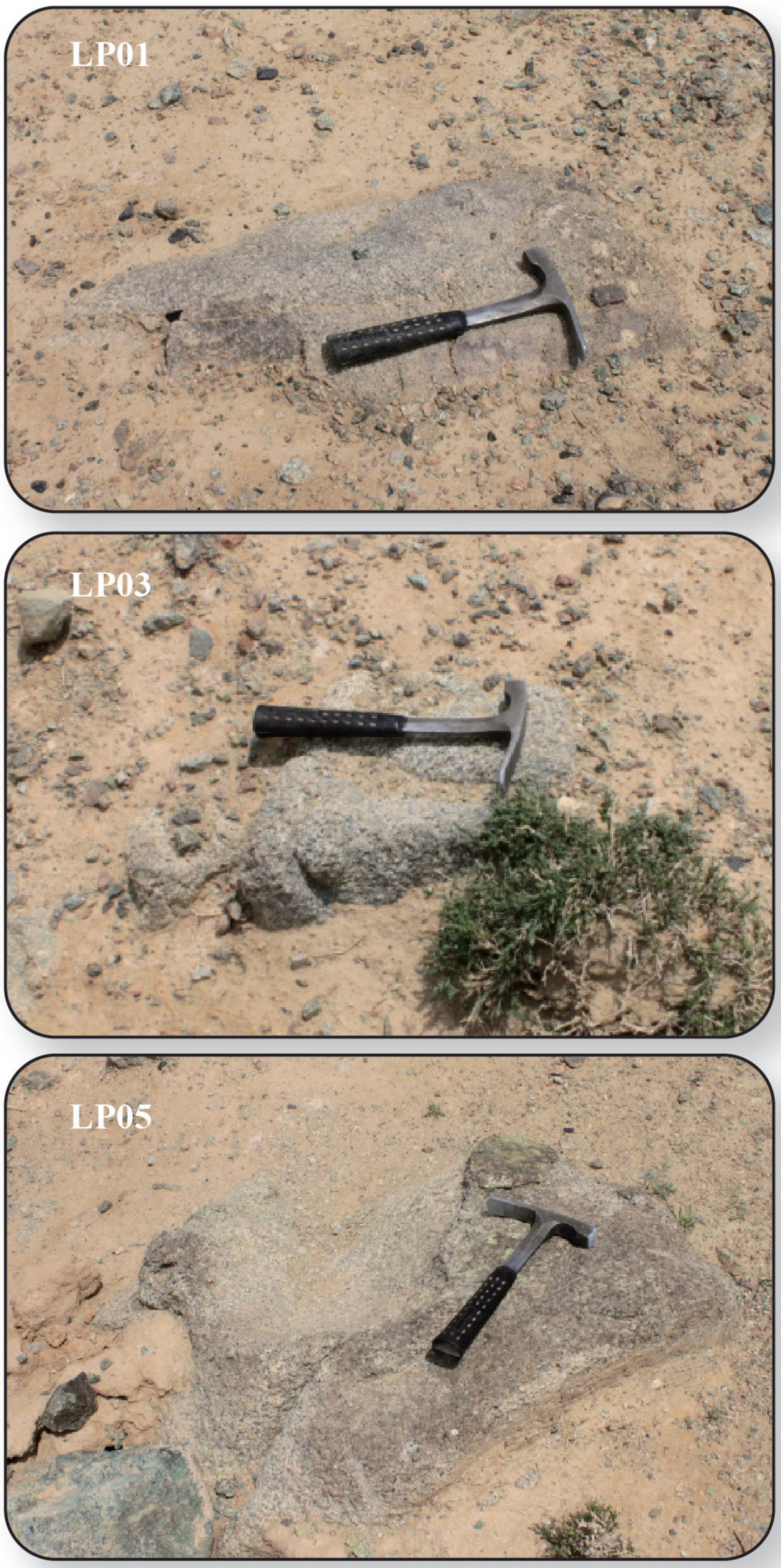
LP01
LP02
LP03
LP04
LP05
LP06

b

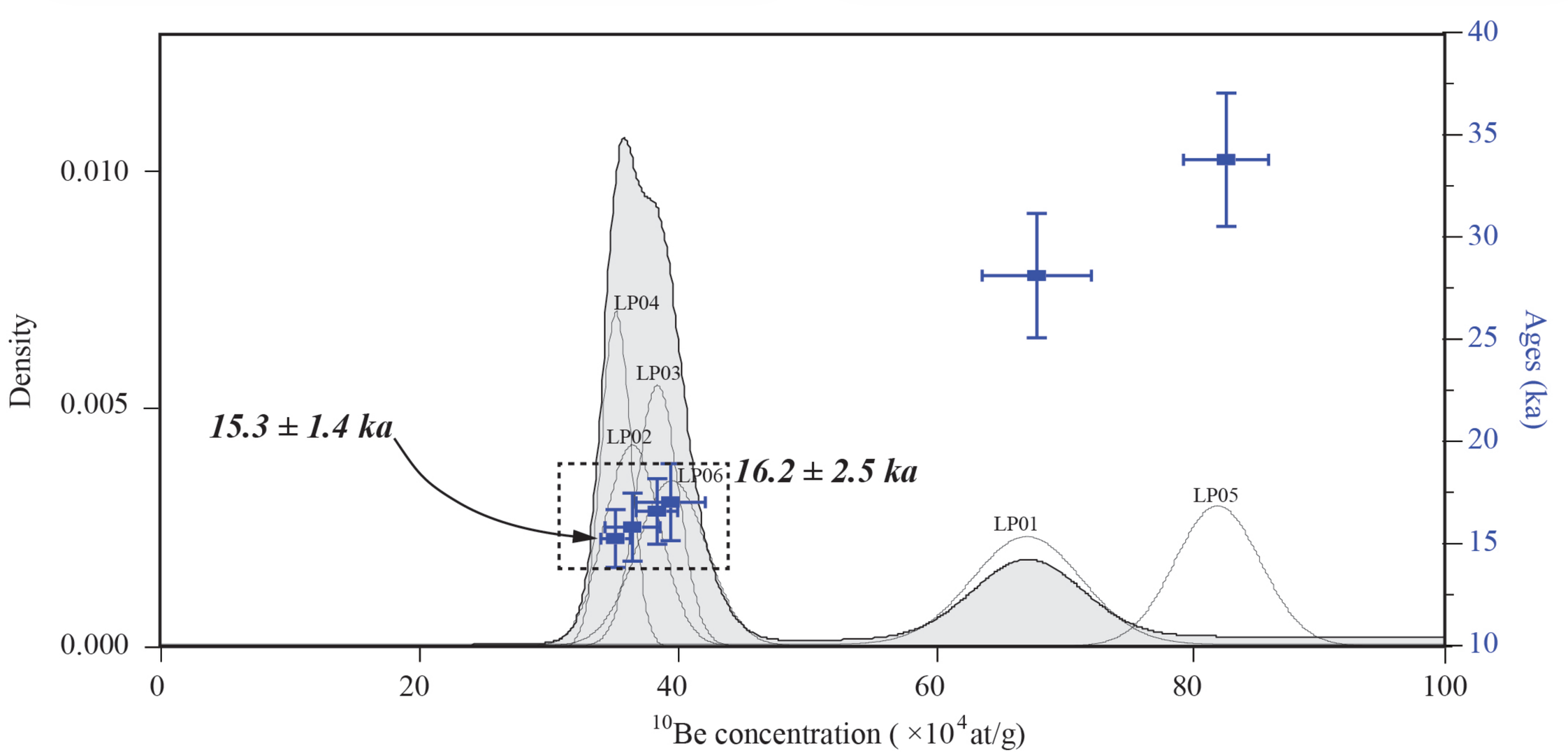
Density
0.010
0.005
0.000
0
20
40
60
80
100
10
15
20
25
30
35
40
Ages (ka)
^{10}Be concentration (×10^{4}at/g)
15.3 ± 1.4 ka
16.2 ± 2.5 ka
LP01
LP02
LP03
LP04
LP05
LP06

Figure 12.

Model 1

200 m
(x4)

8.2°

T4

7.8°

A1

7.8°

T3

7.2°

6.8°

T2

7.3°

T1

6.5°

6.4°

6.5°

5.8°

5.2°

4.9°

reference base level
(profiles p1 and aa')

Model 2

(U)
22m

200 m
(x4)

T4

13m

A2

1.9m

T3

1.5m

T2

T1

1000 m

Figure 13.

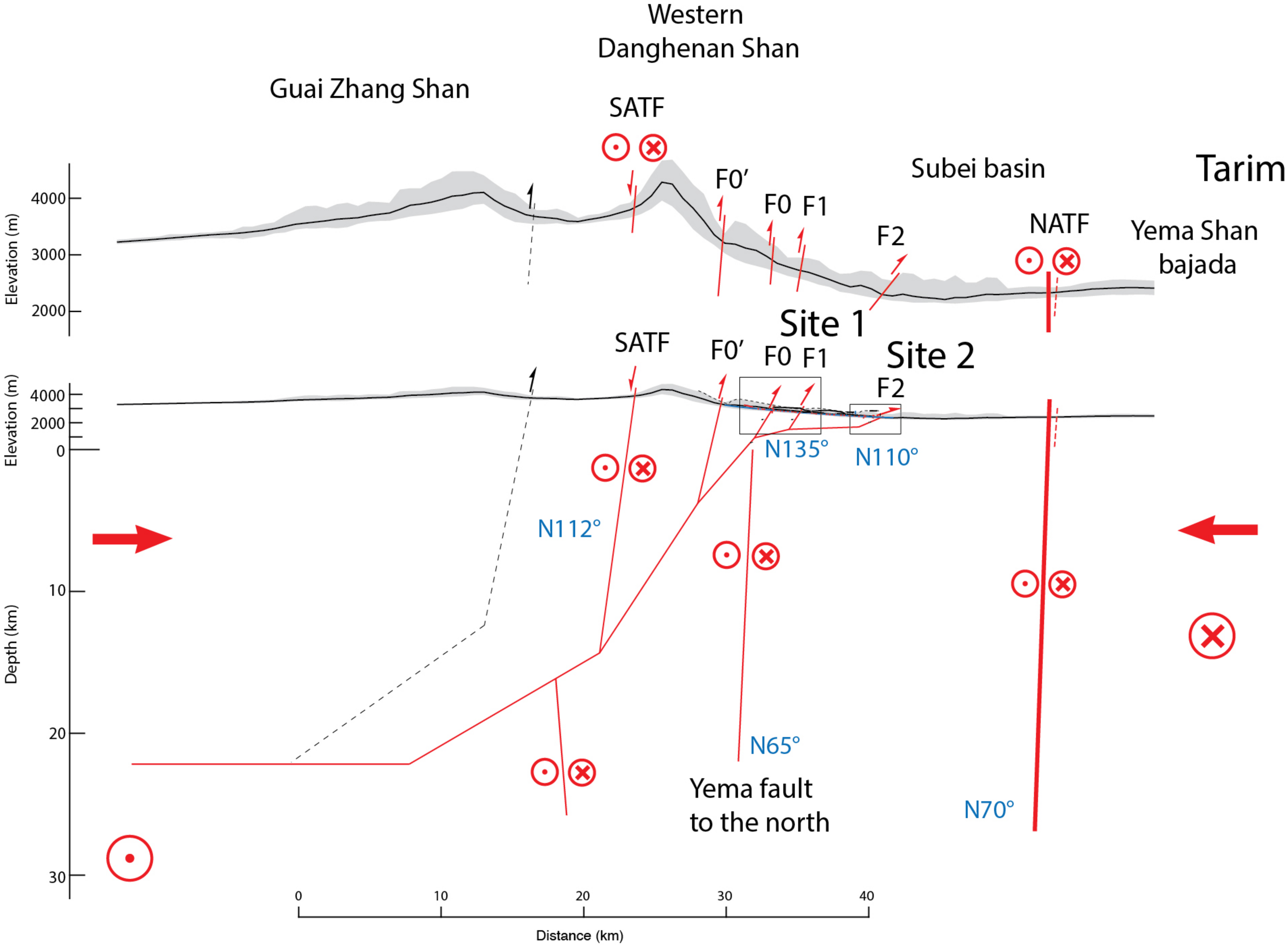

projection N15°

Figure 14.

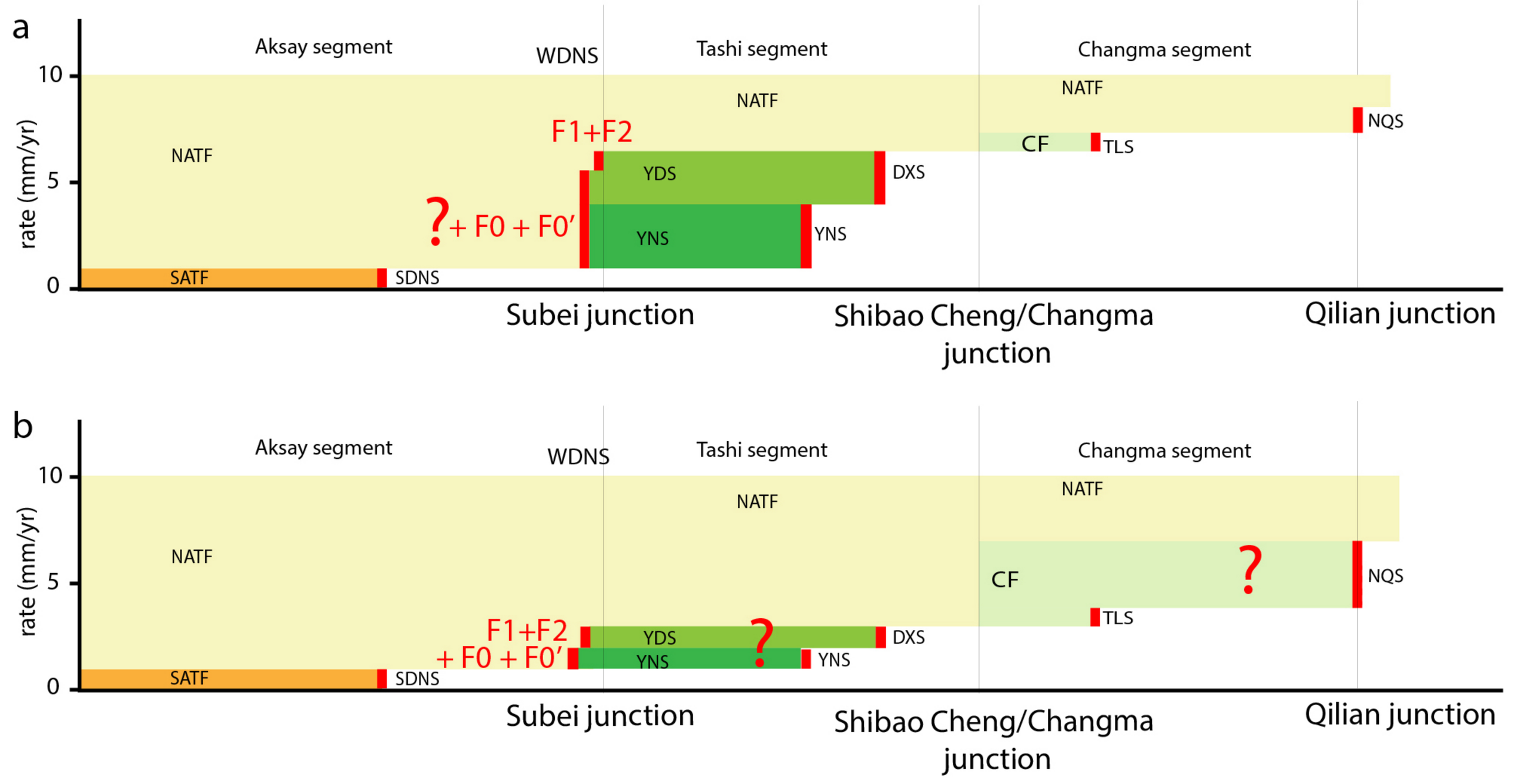
a
Aksay segment
WDNS
Tashi segment
Changma segment
10
5
0
rate (mm/yr)
NATF
NATF
NATF
F1+F2
YDS
DXS
? + F0 + F0'
YNS
YNS
CF
TLS
NQS
SATF
SDNS
Subei junction
Shibao Cheng/Changma junction
Qilian junction
b
Aksay segment
WDNS
Tashi segment
Changma segment
10
5
0
rate (mm/yr)
NATF
NATF
NATF
CF
?
NQS
TLS
F1+F2
+ F0 + F0'
YDS
?
DXS
YNS
YNS
SATF
SDNS
Subei junction
Shibao Cheng/Changma junction
Qilian junction